6 Results

This chapter contains results of thermal-infrared studies of 8 asteroids. Each of the eight sections is devoted to a self-contained study of an individual asteroid. Object-specific aspects of our results are discussed in the appropriate section, implications on asteroid science in general will be discussed in chapter 7.

The first five sections contain our main results: the thermal inertia, size, and albedo of 5 near-Earth asteroids (NEAs) with diameters spanning the range 0.1– 17 km. These results are based on application of our thermophysical model (TPM; see chapter 3) to extensive sets of thermal-infrared data, most of which have been obtained using the IRTF (see chapter 4) or the Spitzer Space Telescope (see chapter 5). Section 6.1, in particular, contains a study of (433) Eros, which had been scrutinized using the NEAR-Shoemaker spacecraft. The primary aim of our Eros study is to validate the TPM for application to NEA data.

Sections 6.6 and 6.7 contain studies of asteroid targets of future spacecraft encounters: (21) Lutetia, target of a flyby of the ESA spacecraft Rosetta in 2010, and (10302) 1989 ML, a nominal target of the planned ESA mission Don Quijote. Based on new thermal-infrared observations, these objects' size and albedo have been determined, their surface mineralogy and thermal inertia have been constrained.

In section 6.8, the first thermal-infrared observations of an eclipsing binary asteroid system, (617) Patroclus, are reported. These allowed us to determine the system's thermal inertia in a fascinatingly direct way.

6.1 (433) Eros [1]

In order to study the applicability of our thermophysical model (TPM) to NEAs, it was used to analyze published high-quality thermal-infrared data (Harris and Davies, 1999) of an extremely well studied object: (433) Eros, the NEA target of the rendezvous mission NEAR-Shoemaker.

---

[1] A preliminary version of the chief result presented herein was prepublished (Mueller et al., 2004). The analysis of Eros data reported therein was entirely done by me.

We obtain a best-fit diameter of 17.8 km, within $\sim$5 % of the NEAR-Shoemaker result of 16.9 km (Thomas et al., 2002). Depending on model assumptions, the best-fit thermal inertia is 100–200 J s$^{-1/2}$K^{-1}m^{-2}, a very plausible value given the boulder-strewn yet regolith-dominated surface structure determined from spacecraft imaging, and furthermore in excellent agreement with previous estimates.

We conclude that the TPM is well suited to be applied to NEA data.

6.1.1 Introduction

Eros is a well studied object. E.g., the NEAR Shoemaker spacecraft scrutinized it for over one year while in orbit around Eros (see Veverka et al., 2000, and references therein). Thomas et al. (2002) report a regolith-dominated surface with a moderate amount of craters and boulders, and a volume of 2535 km^3, corresponding to an effective diameter of 16.9 km (see eqn. 2.1 on p. 28). Eros' disk-integrated albedo is $p_{\mathrm{V}} = 0.29 \pm 0.02$ (at $\lambda = 550$ nm) and $A = 0.12 \pm 0.02$ (Domingue et al., 2002). The exact spin state was determined by Thomas et al. (2002) along with an accurate model of its shape; the latter is available in a computer-readable format on-line at the Planetary Data System (`http://pdssbn.astro.umd.edu/volume/nieros_4001/data/`).

Eros' thermal inertia has not been directly determined from spacecraft measurements. However, Eros was observed extensively during an exceptionally favorable close approach in 1974/75 enabling thermal studies of unprecedented detail (Morrison, 1976; Lebofsky and Rieke, 1979). Although Eros' shape had not been known in detail at that time, the authors could make use of detailed optical lightcurves available to them. Correcting the thermal lightcurve to the optical lightcurve (and allowing for a relative phase shift), Morrison (1976) obtained an upper limit on thermal inertia[2] around 100 J s$^{-1/2}$K^{-1}m^{-2}. Lebofsky and Rieke (1979), on the other hand, fitted a crude shape model to available optical light curves and based a thermophysical model on that shape model. In their thermophysical model, thermal conduction is explicitly modeled whereas beaming is approximated in a rather simple way. They inferred a thermal inertia between 140 and 280 J s$^{-1/2}$K^{-1}m^{-2}, significantly above the lunar value around 50 J s$^{-1/2}$K^{-1}m^{-2}. The database available to Lebofsky and Rieke is a superset of that available to Morrison, they also used a more realistic thermophysical model. We therefore take their thermal-inertia estimate to be more reliable.

---

[2] As was usual at that time, thermal inertia is defined by Morrison as the reciprocal of our definition (eqn. 3.10d on p. 55). Values are given in units of cal^{-1} cm^2 s$^{1/2}$ K.
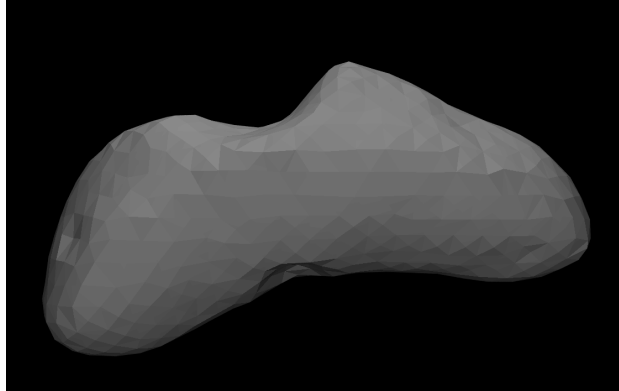
Figure 6.1: Depiction of the Eros shape model by Thomas et al. (2002) used by us. The figure was created using the freeware ray-tracing software POV-ray.

Eros has been reobserved in the thermal infrared by Harris and Davies (1999). From a NEATM analysis, the authors indirectly concluded that Eros' thermal inertia was around 170 J $s^{-1/2}K^{-1}m^{-2}$, well within the range determined by Lebofsky and Rieke (1979).

6.1.2 Modeling

Our thermophysical modeling is based on the model of Eros' shape and spin state by Thomas et al. (2002), the version with 1708 triangular facets is used (see Fig. 6.1). To validate our numerical treatment of the model geometry, we have in a first step attempted to reproduce published optical lightcurves of Eros, finding excellent agreement between synthetic optical lightcurves and published observational data by Hicks et al. (1999) and Erikson et al. (2000).

N-band data are analyzed which were obtained by Harris and Davies on June 27–30 1998 using the United Kingdom Infrared Telescope UKIRT on Mauna Kea / Hawai'i with the CSG3 spectrometer (see Harris and Davies, 1999, for details). There is a total of 7 spectra, each providing simultaneous photometry at 25 wavelengths between 8.06 and 13.04 µm. While Harris and Davies (1999) referred all data to a common observing geometry and to the flux level of lightcurve average, we rather aim at reproducing each spectrum at the time of observation with the corresponding observing geometry. To this end, our TPM (see chapter 3) is used.

Most required input parameters have been determined from NEAR-Shoemaker results (Domingue et al., 2002; Thomas et al., 2002): $H = 10.82$ as implied by $D = 16.9$ km and $p_V = 0.29$, while the p_V-value and the reported Bond albedo

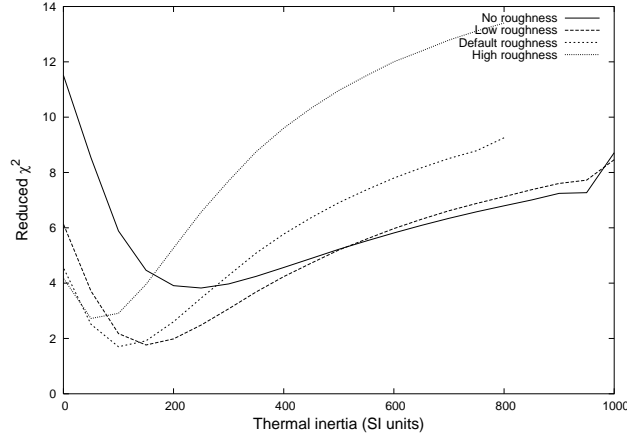**Figure 6.2:** Eros: Reduced χ^2 as a function of thermal inertia for different roughness parameters. With 7×25 data points and two fit parameters (diameter and thermal inertia), the reduced χ^2 equals $\chi^2/173$.

imply $G = 0.181$ (see eqn. 2.2 on p. 28). The J2000 ecliptic coordinates of the spin axis are $\beta = +11.35°$, $\lambda = 17.22°$, implying a subsolar latitude at the time of the UKIRT observations of $+34°$, a sub-Earth latitude of $\sim +64°$, and an hour angle of the Sun at the sub-Earth point of $+0.9$ h corresponding to a "local time" of 12.9 h, i.e. the afternoon side was observed.

6.1.3 Results

See Figures 6.2 and 6.3 for plots of the best-fit χ^2 and diameters as a function of thermal inertia, using the methods detailed in sect. 3.5. Both figures contain slight "wiggly" artefacts for large thermal-inertia values due to the approximation mentioned therein; these artefacts quickly become unnoticeable with decreasing thermal inertia. The respective scale factor, κ, is closely related to the derivative of the curves given in Fig. 6.3, which are seen to be relatively flat; it has been verified that κ is within 1 % of unity for all but the lowest and largest thermal-inertia values considered. To increase the numerical accuracy at low thermal inertia, one may decrease the step size in thermal inertia.

As apparent from Fig. 6.2, the best-fit thermal inertia is dependent on the assumed roughness parameters, where increasing roughness decreases the best-fit thermal inertia. The data are best fit for intermediate roughness parameters, roughly in the range of 100–200 J s$^{-1/2}$K^{-1}m^{-2} in thermal inertia.

As can be seen in Fig. 6.3, the best-fit diameter for low roughness and a thermal inertia of 150 J s$^{-1/2}$K^{-1}m^{-2} (the best-fit value for these roughness parameters) is
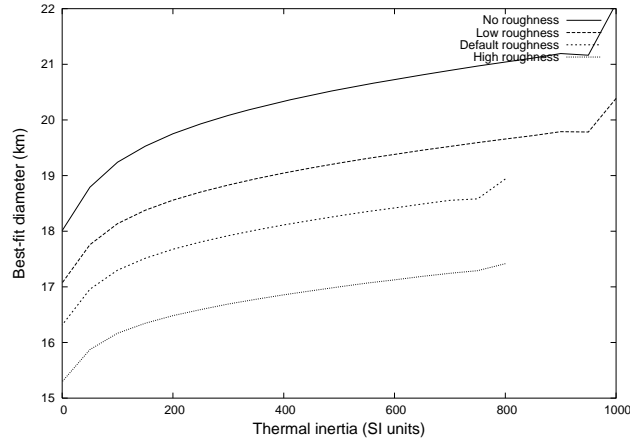
Figure 6.3: Eros: Best-fit diameter as a function of thermal inertia for different roughness parameters.

around 18.3 km, while for default roughness the best-fit diameter is $\sim$ 17.3 km.

6.1.4 Discussion

The best-fit diameter is slightly model dependent, but within the range 17.8 ± 0.5 km, where the quoted uncertainty reflects solely the statistical scatter inherent in the data and the systematic uncertainty from the unknown roughness parameters. Other sources of uncertainty, which are hard to estimate *a priori* but are probably dominated by systematic modeling uncertainties, add to the error budget. The NEAR-Shoemaker result is 16.9 km (Thomas et al., 2002), some 5 % below our result.

The best-fit thermal inertia is 100–200 J $s^{-1/2}K^{-1}m^{-2}$, in excellent agreement with previous estimates by Lebofsky and Rieke (140–280 J $s^{-1/2}K^{-1}m^{-2}$) and Harris and Davies ($\sim$ 170 J $s^{-1/2}K^{-1}m^{-2}$). We reckon that our result supersedes previous estimates since it makes explicit use of Eros' spin state and shape model determined from the NEAR-Shoemaker spacecraft.

Eros' thermal inertia is more than an order of magnitude below that of bare rock and roughly three times the lunar value (see table 3.1 on p. 58), a very plausible value given spacecraft imaging of Eros' surface, which reveal a regolith-dominated surface with a moderate amount of craters and boulders (Thomas et al., 2002); the latter being consistent with the higher-than-lunar thermal inertia.

We conclude that applying our TPM, based on a detailed shape model, to published thermal-infrared data of Eros results in estimates for diameter and thermal

inertia which are in excellent agreement with previous estimates including "ground truth" from spacecraft observations. In particular, the diameter uncertainty due to systematic modeling uncertainties does not appear to vastly exceed 5 % for the favorable circumstances (large data set, accurate model of shape and spin state, moderate solar phase angle of 29°) of this study. No such studies for an NEA have been published before.

Eros' shape model by Thomas et al. (2002) is not convex but contains several prominent concavities (see Fig. 6.1 on p. 139). Nevertheless, the convex-shape TPM produces results in excellent agreement with independently obtained results. This is somewhat unexpected because the indentations present on Eros' surface would be expected to lead to shadowing effects and to mutual heating of surface elements as discussed in chapter A in the appendix. We conclude that neglecting the effects of non-convex global shape does apparently not lead to a critical systematic diameter offset for objects as irregularly shaped as Eros.

In general, neglecting shadowing leads to an overestimation of thermal flux and consequently to a diameter underestimation; the converse applies to neglecting mutual heating. The fact that our derived diameter is slightly larger than the spacecraft result may indicate that at the moderate phase angle of the considered observations ($\sim 29°$) the effect of mutual heating dominates the cooling effect of shadowing, which may become more relevant at larger phase angles. Further analysis using a more general TPM accounting for shadowing and mutual heating are required to study this speculation.

We would expect more accurate constraints on Eros' physical properties to result from a TPM fit to all thermal-infrared data available in the literature, including the flux values quoted in Lebofsky and Rieke (1979), such that the database would stretch a broader range in solar phase angle and aspect geometry. Note that, in contrast to simple models, our model can be used to consistently fit data obtained at different epochs. However, combining data obtained by different observers using different instruments requires a very careful assessment of potential cross-calibration issues and of the relative accuracies of the data sets, which is beyond our current scope.

6.1.5 Summary

In order to validate our TPM for application to NEAs, thermal-infrared observations (Harris and Davies, 1999) of the NEA (433) Eros have been reanalyzed. Eros had been scrutinized from ground and through the NEAR-Shoemaker spacecraft.

Eros' diameter is reproduced to within $\sim 5\,\%$ of the NEAR-Shoemaker result (Thomas et al., 2002). The best-fit thermal inertia is 100–200 J s$^{-1/2}$K^{-1}m^{-2} depending on the assumed model roughness parameters, in excellent agreement with earlier estimates. Eros' thermal inertia is more than an order of magnitude below that of bare rock and roughly three times the lunar value, a very plausible value given Eros' surface structure as revealed by spacecraft imaging.

We conclude that our convex-shape TPM is well suited to analyze thermal-infrared observations of NEAs and to derive quantitative estimates of their diameter, albedo, and thermal inertia.

6.2 (25143) Itokawa [3]

In 2005, the Japanese spacecraft Hayabusa has rendezvoused with the NEA (25143) Itokawa. Prior to that, in 2004, we had performed thermal-infrared observations of Itokawa with the IRTF and MIRSI, which are presented here. Preliminary results have been accepted for publication in the proceedings of the 1st Hayabusa symposium (Mueller et al., 2004), which has not yet been printed, however.

Additional thermal-infrared observations were published by Müller et al. (2005),[4] also before the arrival of Hayabusa. There included is a recalibration of other data points found in the literature, which he had used in our preliminary analysis.

We here present TPM analyses of different combinations of thermal-infrared data sets, including the first analysis of the complete set of reliable thermal data of Itokawa. The resulting best-fit diameter is 0.32–0.33 km, in excellent agreement with Hayabusa results. Together with the results of our Eros study (see sect. 6.1), this suggests that the systematic diameter uncertainty inherent in our thermophysical modeling does not exceed 10 %.

Itokawa's thermal inertia is found to be 700 ± 100 J s$^{-1/2}$K^{-1}m^{-2}, refining the estimate by Müller et al. (2005), 750 ± 250 J s$^{-1/2}$K^{-1}m^{-2}.

---

[3] A preliminary version of the results herein were prepublished (Mueller et al., 2004). The new ESO observations reported therein were performed and reduced by Marco Delbo' and Mario di Martino (Delbo', 2004), the new IRTF observations were performed and reduced by myself. The thermophysical modeling of the data set was performed by myself.

[4] In an attempt to reduce confusion, Thomas Müller, MPG Garching, is spelled Müller (with umlaut) throughout this thesis, while my last name is spelled Mueller (no umlaut).

6.2.1 Introduction

(25143) Itokawa (previously known as 1998 SF36) is an S-type NEA which is a particularly favorable spacecraft target due to the relatively moderate amount of energy and time required to reach it. It has been studied in detail from the spacecraft Hayabusa during a rendezvous in 2005 (see Fujiwara et al., 2006, and references therein). Apart from a detailed study of the asteroid's physical properties using remote sensing techniques while hovering within a few kilometers of the asteroid surface, Hayabusa was scheduled to take small samples of asteroid material and to return them to Earth. Due to technical problems it is currently unclear whether Hayabusa has succeeded in taking samples and whether it will manage to return to Earth; the planned Earth-arrival date is in 2010.

We have observed Itokawa at the IRTF in July 2004, before the arrival of Hayabusa at its target. Apogee data obtained by us have been used by Kaasalainen et al. (2004a) in the derivation of Itokawa's shape and spin state. Our MIRSI data, combined with other data found in the literature, have been used by us to determine Itokawa's size and thermal inertia.

A vast body of information on Itokawa has been collected both before and after the arrival of Hayabusa using different techniques, we here focus on those which are most relevant for our purposes, i.e. estimates of size, shape, and thermal inertia.

6.2.1.a Pre-Hayabusa

Sekiguchi et al. (2003) report single-wavelength N-band photometry and estimate the diameter of Itokawa to be 0.35 ± 0.03 km, using the STM (see sect. 2.4.1). Combining the Sekiguchi et al. flux measurement with newly obtained M′-band photometry at 4.68 µm, Ishiguro et al. (2003) derive dimensions for a triaxial ellipsoid of $(620 \pm 140) \times (280 \pm 60) \times (160 \pm 30)$ m, corresponding to an effective diameter of roughly 300 ± 30 m. Ishiguro et al. also report a thermal inertia of 290 J s$^{-1/2}$K^{-1}m^{-2}, which they derive from the two thermal-infrared data points at their disposal. Their thermal model assumes a spherical shape.

From radar observations, Ostro et al. (2004) determine a shape model of Itokawa and a volume-equivalent diameter of 358 ± 36 m. After obtaining new radar observations in June 2004, Ostro et al. (2005) publish an updated shape model and size estimate, with ellipsoidal axes within 10 % of $594 \times 320 \times 288$ m, corresponding to a volume-equivalent diameter of 380 ± 38 m.

Kaasalainen et al. (2004a) determined the spin state of Itokawa and a convex-

Table 6.1: Itokawa: Overview of published diameter estimates, D, and reported uncertainties, σ.

D(km)	σ(km)	Source
0.35	0.03	Sekiguchi et al. (2003)
0.30	0.03	Ishiguro et al. (2003)
0.36	0.04	Ostro et al. (2004)
0.38	0.04	Ostro et al. (2005)
0.28	—	Mueller et al. (2004)
0.32	0.03	Müller et al. (2005)
0.327	0.006	Demura et al. (2006)

definite model of its shape from the inversion of optical lightcurve data.

From a preliminary analysis of the thermal-infrared data published by Sekiguchi et al. (2003) and Ishiguro et al. (2003), and new data which had been obtained at the ESO 3.6-m telescope (later published in Delbo', 2004) and at the IRTF (see below), we (Mueller et al., 2004) determined a diameter around 280 m and a thermal inertia of some 350 J s$^{-1/2}$K^{-1}m^{-2}. Our analysis was based on the Kaasalainen et al. (2004a) shape model and the TPM described in chapter 3. The thermal-inertia result is intermediate between lunar regolith and bare rock (but closer to the former) and was interpreted as "incompatible with a surface dominated by bare rock." An Eros-like surface was proposed but with a coarser regolith and/or a larger number of boulders.

Müller et al. (2005) obtained further thermal-infrared flux measurements at the ESO 3.6-m telescope. Combining their data with those of Sekiguchi et al. (2003) and Delbo' (2004) but with neither our MIRSI data (which were not available to them) nor the Ishiguro et al. (2003) M-band value, they determined a diameter of 0.32 ± 0.03 km and a thermal inertia of 750 J s$^{-1/2}$K^{-1}m^{-2}, which they interpret as "an indication for a bare rock dominated surface." Their results are based on the thermophysical model by Lagerros (1996, 1997, 1998a) and the shape model by Kaasalainen et al. (2004a) which had also been used by us.

6.2.1.b Hayabusa results

From Hayabusa observations, Demura et al. (2006) determined a volume within 5 % of 0.018378 km^3, corresponding to a volume-equivalent diameter of 327 ± 6 m (see eqn. 2.1). See table 6.1 for an overview of published diameter estimates.

Demura et al. also report an updated shape model which appears to be in broad agreement with that by Kaasalainen et al. (2004a), however at the time of writing it has not yet been released to the scientific community.[5] A spin axis is reported within 3.9° of $\lambda = 128.5°$ and $\beta = $ -89.66° (J2000 ecliptic coordinates), in very good agreement with the estimate by Kaasalainen et al. (2004a).

From global imaging of Itokawa (see, e.g., Fig. 1.1 on p. 2) one recognizes a dichotomy between rough and smooth terrains on Itokawa's surface, which cover some 80 and 20 % of the surface area, respectively (Saito et al., 2006). Rough terrains are densely covered in boulders of various sizes, in contrast to smooth areas which display very low boulder abundance.

During operations in preparation of the spacecraft touchdowns for sample taking and during the two touchdowns themselves, high-resolution imaging was obtained of the vicinity of the touchdown sites, i.e. of parts of the Muses-C region and of adjacent rough terrain (Yano et al., 2006). The obtained images of smooth terrain display a dense cover of coarse regolith consisting of gravel in the mm–cm range with no apparent sign of finer dust on the surface. Itokawa's regolith is coarser than the regolith found in Eros' ponds (Yano et al., 2006). The smooth regolith-covered regions were found to coincide with the minima of the gravitational potential (see Fujiwara et al., 2006). Based on an analysis of high-resolution imaging, Miyamoto et al. (2007) report evidence for "landslide-like granular migration" on Itokawa's surface, i.e. for regolith migration aligned with the local gravity slope. They conclude that Itokawa's surface is unconsolidated and suggest that vibrations due to, e.g., impact-induced seismic shaking cause gravel fluidization and subsequent down-slope movement, where the resulting grain mobility increases with decreasing grain size.

A very low abundance of crater-like features was found on Itokawa's surface, totaling no more than 100 for crater diameters exceeding 70 cm (see Saito et al., 2006). Craters of small and intermediate size may be buried in migrating regolith; Miyamoto et al. (2007) present images of regolith concentrations on the floors of crater-like features.

One estimate of a local value of thermal inertia is available, obtained from an indirect temperature measurement during touchdown. The temperature close to the sampling site in the Muses-C terrain is estimated by Yano et al. (2006) to be 310 ± 10 K, which they conclude is indicative of a thermal inertia in the

---

[5] The Hayabusa data archive including an update on the shape model by Demura et al. (2006) has been made public on 24 April 2007 (see `http://hayabusa.sci.isas.jaxa.jp/`).

Table 6.2: Flux values resulting from MIRSI observations of Itokawa on 10 July 2004 (UT). Times given refer to the middle of the exposure and are corrected for 1-way light-time.

Time (h)	Wavelength (µm)	Flux $\left[\frac{10^{-15}\text{W}}{\text{m}^2\mu\text{m}}\right]$	σ flux $\left[\frac{10^{-15}\text{W}}{\text{m}^2\mu\text{m}}\right]$
11.73888	11.7	16.7	2.2
11.79576	11.7	15.8	2.0
13.52352	11.7	20.0	2.5
13.67784	9.8	24.7	3.9
13.84128	9.8	17.8	3.8

range between 100 and 1000 J s$^{-1/2}$K^{-1}m^{-2}, although there appear to be significant systematic uncertainties in their thermal modeling.

6.2.2 Thermal-infrared observations

We have observed Itokawa with the NASA IRTF (see chapter 4) on Mauna Kea / Hawai'i using MIRSI and Apogee on 10 July 2004 (UT). The Apogee data are not needed here, hence they shall be disregarded in the following. Additional observations were scheduled for 28 and 29 July but failed due to bad weather. The night of 10 July was photometric but had a relatively high (constant) level of atmospheric humidity.

During our observations, Itokawa's heliocentric distance was 1.06 AU, its topocentric distance from Mauna Kea was 0.05 AU, the solar phase angle was 28.3°. Itokawa's declination was −40°, the airmass at meridian transit (∼ 12:15 UT) was 2.0. Unfortunately, technical problems[6] disabled MIRSI observations for some 90 minutes around transit, hence the reported MIRSI observations have been obtained at larger airmasses. The Cohen et al. (1996, 1999) calibration standard stars β And and α Lyr have been observed at similarly large airmasses before and after the Itokawa observations. MIRSI data have been reduced using the methods described in sect. 4.4; see table 6.2 for the resulting flux values.

In Mueller et al. (2004), preliminary TPM fits are reported based on the MIRSI data quoted in table 6.2, thermal fluxes obtained at the ESO 3.6-m telescope with TIMMI2 on 8 April 2001 (Delbo', 2004, measurements from 9 April are also reported but were not used due to the reported unfavorable atmospheric conditions

---

[6] This was the first occurrence of the MIRSI "striping" artefact visible in Fig. 4.3 on p. 91, which hit us unexpectedly at the time of the Itokawa observations.

in that night), and respectively one thermal flux value from Sekiguchi et al. (2003, 11.9 µm photometry obtained with TIMMI2) and Ishiguro et al. (2003, 4.68 µm photometry obtained at Subaru). Later, we were informed that the 4.68 µm flux value reported by Ishiguro et al. was likely to be compromised (Hasegawa, 2004, private communication; Hasegawa is a co-author of that paper).

The database of Müller et al. (2005) contains new TIMMI2 measurements in addition to those used by us (Delbo' and Sekiguchi et al.). Our MIRSI data were not available to them. They chose not to use the 4.68 µm flux by Ishiguro et al. Flux values originally reported by Delbo' and Sekiguchi et al. have been recalibrated by Müller et al.

We have used our TPM described in chapter 3 to fit different combinations of data sets. Itokawa's absolute optical magnitude is assumed to be $H = 19.5$ throughout our analysis, which appears to be consistent with our Apogee data. The exact choice of H would be expected to have negligible influence on diameter and thermal-inertia results. The following data sets are analyzed:

1. That considered in Mueller et al. (2004), i.e. MIRSI data, TIMMI2 data by Delbo' (8 April 2001) + Sekiguchi et al., and M-band data by Ishiguro et al. Unlike in Mueller et al. (2004), recalibrated TIMMI2 fluxes are used. (total: 12 data points)

2. As above, but without the Ishiguro et al. M-band data: MIRSI + recalibrated TIMMI2 data by Delbo' and Sekiguchi et al. (total: 11 data points)

3. The "high-quality" data points reported in Müller et al. (2005), including Delbo' and Sekiguchi et al. data as above. (total: 15 data points)

4. All reliable data, i.e. the 15 data points as above in addition to our MIRSI data. (total: 20 data points)

6.2.3 Results

See Figures 6.4, 6.5, 6.6, and 6.7 for our model analyses of the four data sets described above. See sect. 6.1 for a detailed discussion of analogous plots and their interpretation. Our results for the individual data sets are:

1. Depending on roughness parameters, χ^2 is minimized at very different thermal-inertia values. Thermal inertia is not well constrained by the data, although values much below 250 J s$^{-1/2}$K^{-1}m^{-2} would appear to be inconsistent. The
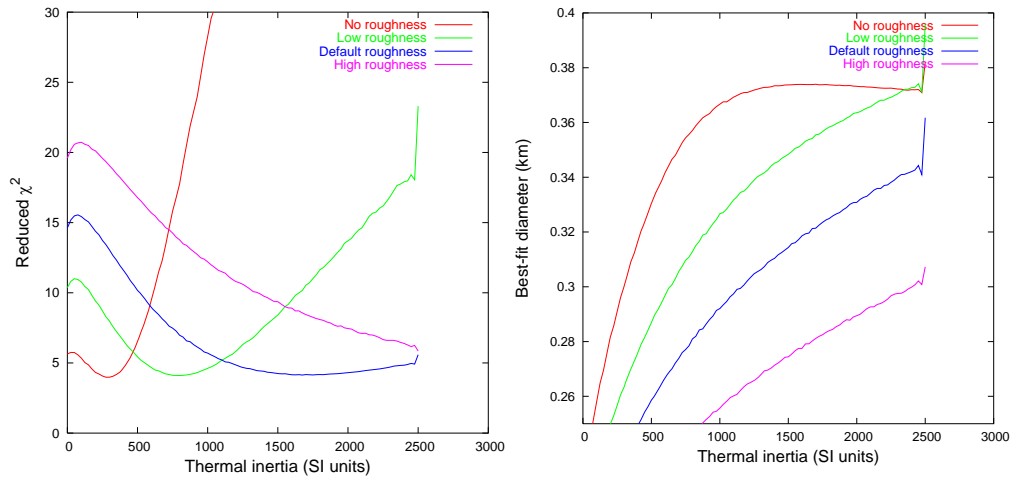
Figure 6.4: Itokawa: TPM fits to data set 1, i.e. the flux values considered in Mueller et al. (2004). Left: Reduced χ^2 as a function of thermal inertia for four sets of roughness parameters (see sect. 3.5). Right: Best-fit diameter as a function of thermal inertia.
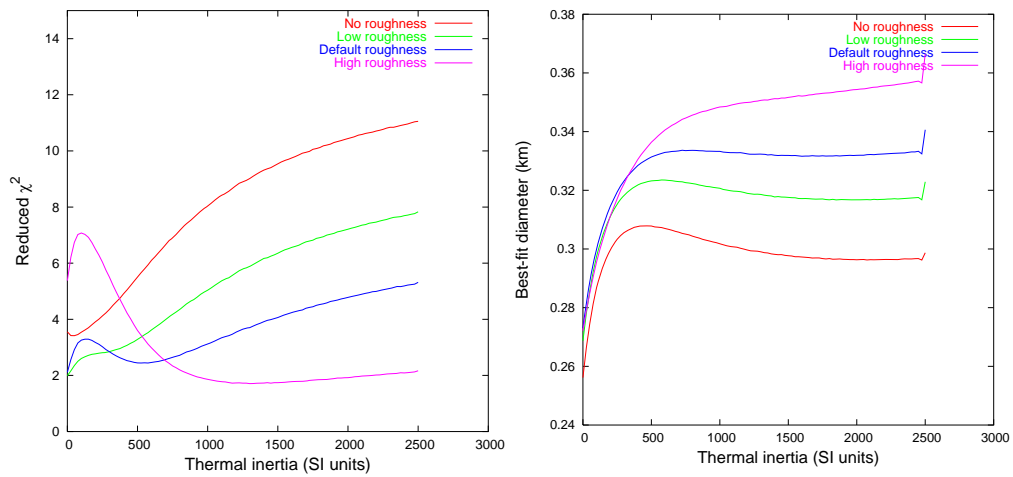

Figure 6.5: As Fig. 6.4, but without the 4.68 µm flux value reported by Ishiguro et al. (2003) (data set 2).
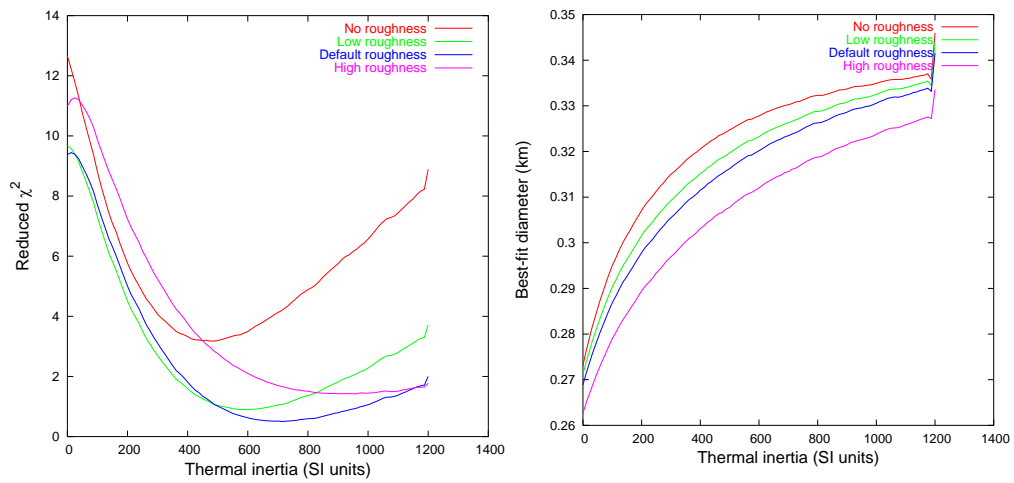
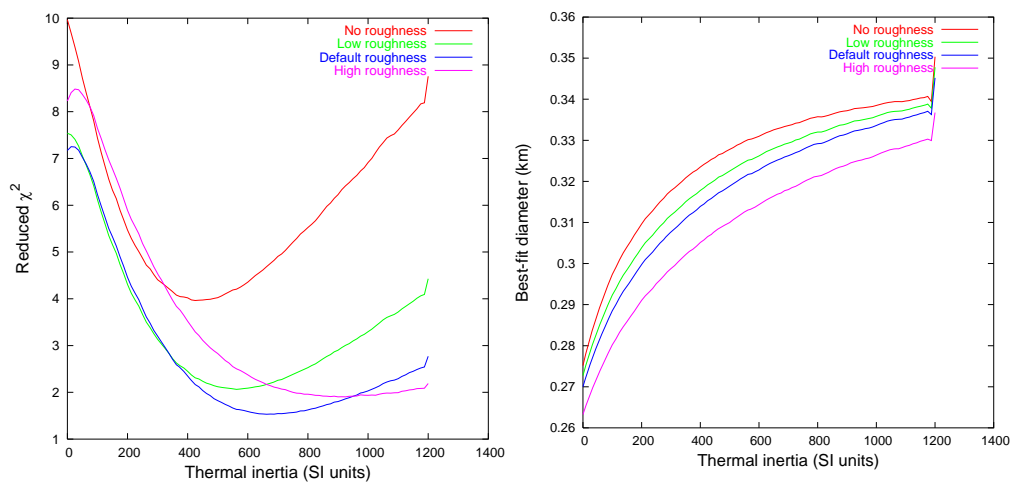**Figure 6.6:** As Fig. 6.4, but for the data set quoted by Müller et al. (2005) (data set 3).

Figure 6.7: As Fig. 6.4, but for the complete set of reliable thermal-infrared data, i.e. those quoted by Müller et al. (2005) in addition to the MIRSI data given in table 6.2 (data set 4).

corresponding best-fit diameters vary between 296 m (no roughness, $\Gamma =$ 275 J s$^{-1/2}$K^{-1}m^{-2}) and 319 m (default roughness, $\Gamma =$ 1650 J s$^{-1/2}$K^{-1}m^{-2}). The difference in best-fit diameter when compared to Mueller et al. (2004) is due to the recalibration of the ESO fluxes discussed above. Fitting the data for individual sets of roughness parameters clearly shows that there is no well constrained global χ^2 minimum. This was somewhat obscured by the approach used in Mueller et al. (2004), where crater density was used as a variable fit parameter.

2. Thermal inertia is unconstrained within the range 0–2500 J s$^{-1/2}$K^{-1}m^{-2}, the largest value considered in our analysis (thermal inertia of bare rock). Zero roughness appears to be a poor fit to the data, but none of the remaining three roughness models is excluded. The corresponding best-fit diameters vary between 0.27 and 0.35 km. Note that by disregarding a single data point we could significantly improve the quality of the fit: the reduced χ^2 now reaches much lower values than for data set 1.

3. There is a clear global minimum for "default" roughness at thermal-inertia values between 600 and 800 J s$^{-1/2}$K^{-1}m^{-2}, although slightly lower values (Γ between 500 and 700 J s$^{-1/2}$K^{-1}m^{-2}) and "low" roughness are not ruled out. Zero and "high" roughness would appear to be less consistent with the data. For the quoted ranges in thermal inertia, the corresponding best-fit diameters vary between 0.320 and 0.326 km.

4. The global minimum for "default" roughness and thermal inertia between 600 and 800 J s$^{-1/2}$K^{-1}m^{-2} remains, "low" roughness is less well consistent with the data than before. The corresponding best-fit diameters vary between 0.323 and 0.329 km.

These results are summarized in table 6.3.

6.2.4 Discussion

6.2.4.a Diameter

Taken at face value, the best-fit diameter resulting from our TPM analysis of all available reliable thermal-infrared data is 326 ± 3 m, in amazingly good agreement with the Hayabusa result of 327 ± 6 m (Demura et al., 2006). We caution, however, that solely the scatter in the flux values is reflected in the quoted range of uncertainty. Systematic flux calibration uncertainties and systematic uncertainties

Table 6.3: Itokawa: Results of TPM fits to the four data sets considered (see Figs. 6.4–6.7).

Data set	Diameter (m)	Thermal inertia $(\mathrm{J\ s^{-1/2}K^{-1}m^{-2}})$
1	296–319	≥ 250
2	270–350	0–2500
3	320–326	500–800
4	323–329	600–800

inherent in our TPM and in the shape model add to the error budget. Nevertheless, this close match emphasizes the potentially very high accuracy of diameter estimates derived from TPM analysis of a suitable thermal-infrared database. Combining this with results from an analysis of Eros data (see also sect. 6.1), where we were able to reproduce the diameter estimate derived from spacecraft measurements to within ~ 5 %, we conclude that 10 % is a conservative upper limit on the systematic diameter uncertainty inherent in our thermophysical modeling (see sect. 7.2), resulting in a final diameter result of 0.32 ± 0.03 km.

We note that our preliminary results reported in Mueller et al. (2004) were plagued by inaccuracies in flux values quoted from other sources. Using recalibrated TIMMI2 flux values resolves the diameter discrepancy between our preliminary analysis ($D \sim 0.28$ km) and the Hayabusa result, 0.327 ± 0.006 km rejecting the unreliable (Hasegawa, 2004, private communication) M-band flux by Ishiguro et al. significantly increased the goodness of fit.

6.2.4.b Thermal inertia

The best-fit thermal inertia is 700 ± 100 J s$^{-1/2}$K^{-1}m^{-2}. This refines the estimate by Müller et al. (2005, 750 ± 250 J s$^{-1/2}$K^{-1}m^{-2}), which was based on a subset of the database available to us. A reanalysis of their data set confirms their result.

The TPM-derived thermal-inertia result is significantly larger than the estimate by Ishiguro et al. (2003) of ~ 290 J s$^{-1/2}$K^{-1}m^{-2}. This is not entirely surprising given the small data set of only two thermal-infrared data points available to them. Furthermore, Ishiguro et al. analyzed their data using a simplistic thermal model based on spherical geometry which we would expect to be inappropriate for a quantitative determination of thermal inertia.

6.2.4.c Geological interpretation of thermal inertia in the light of Hayabusa results

A thermal inertia of 700 ± 100 J s$^{-1/2}$K^{-1}m^{-2} corresponds to some 14 times the lunar value, so Itokawa's surface would not be expected to be dominated by fine Moon-like regolith. On the other hand, 700 J s$^{-1/2}$K^{-1}m^{-2} is less than a third of the thermal inertia of solid rock (see table 3.1 on p. 58). As highlighted by Müller et al. (2005), Itokawa's corresponding thermal conductivity is $\kappa \sim 0.3$ W K^{-1}m^{-1} which they conclude is a plausible value for "porous stony material".[7] As can be seen from table 3.1, an extremely large porosity would be required to explain this conductivity: 0.3 is smaller than the value for solid rock by a factor of ten, and only twice as large as the value for the very vesicular material pumice, which is an implausible model for asteroidal "bare rock".

Among the materials listed in table 3.1, the best matches to Itokawa's thermal inertia are compact snow, sandy soil, and coal. Given Itokawa's taxonomic classification as S type, sandy soil would be expected to be the best analogue, although we caution that the atmosphere (and furthermore humidity inside the soil) skew thermal-inertia values measured on Earth towards larger values relative to asteroid surfaces.

We note that the thermal skin depth (eqn. 3.10a on p. 55), i.e. the length scale for the penetration of the diurnal heat wave, is of the order of several centimeters given our thermal-inertia result. Gravel with grain sizes up to some 10 cm would therefore be expected to display a reduced thermal inertia relative to boulders made of the same material. Furthermore, a dust coating (thin compared to the skin depth) would reduce the thermal inertia of a boulder. This will be further discussed in sect. 7.3.3.c.

Based on Hayabusa measurements obtained while descending to a sampling site in smooth terrain, a local thermal-inertia value between 100 and 1000 J s$^{-1/2}$K^{-1}m^{-2} was obtained (Yano et al., 2006). The sampling site was seen from close-up imaging to be covered with coarse regolith, with typical grain sizes in the mm–cm range. It is reasonable to expect the sampling site to be representative of Itokawa's smooth terrains, which cover some 20 % of the total area (see Saito et al., 2006). For the rough terrains, which cover some 80 % of the surface area, no local thermal-inertia measurement is available. A small fraction of the rough terrain, adjacent to the touchdown site in the smooth Muses-C region, was imaged in high resolution; the

---

[7] Thermal inertia is proportional to the square root of the mass density, which further decreases the thermal inertia of porous material. The effect of thermal conductivity dominates, however.

images reported by Miyamoto et al. (2007) show much larger grain sizes than in smooth terrain. While particle sizes for the rough terrain are not explicitly reported by Miyamoto et al., their Fig. 2c appears to display a very low abundance of pebble-sized gravel but rather appears to be dominated by larger cobbles which are comparable to the thermal skin depth (centimeters) in size.

From our global thermal-inertia result it appears that the typical thermal inertia on Itokawa's surface does not greatly exceed that of the sampling site, although we caution that the latter is only poorly constrained so far. We speculate that the large boulders apparent in Hayabusa imaging of the rough terrain (see, e.g., Saito et al., 2006, Figs. 3 and 4) are covered with a thin dust coating. Alternatively, the "bare rock" of which Itokawa's boulders are composed may be a poor thermal conductor relative to granite found on Earth; this could be caused by, e.g., a high amount of porosity at length scales smaller than the skin depth, i.e. at the mm-scale or smaller. Note that Christensen et al. (2003) report a thermal inertia up to 2200 J $s^{-1/2}K^{-1}m^{-2}$ for outcrops of exposed bedrock on Mars (the floor of the Nili Patera caldera).

We wish to stress that the dependence of thermal inertia on grain size, which is well established for the atmospheric pressures prevalent on Earth (see Clauser, 1995) and Mars (see Presley and Christensen, 1997), is significantly less well studied in a vacuum. Laboratory measurements of the thermal inertia of particulate materials in a vacuum chamber would be very valuable for the interpretation of our results. The same applies to the effect of porosity on thermal inertia—note that the residual atmospheric gas inside pores enhances the thermal conductivity and hence the thermal inertia.

6.2.4.d Mutual consistency of thermophysical models

The data set of 15 flux values considered by Müller et al. (2005) to be of "high quality" has been reanalyzed. While Müller et al. used the TPM by Lagerros (1996, 1997, 1998a) in their analysis, we use that described in chapter 3 which is largely based on Lagerros' but has been implemented independently.

They report $D = 0.32 \pm 0.03$ km and $\Gamma = 750$ J $s^{-1/2}K^{-1}m^{-2}$. No formal thermal-inertia uncertainty is given, but values between 500 and 1000 J $s^{-1/2}K^{-1}m^{-2}$ are reported to be consistent with their data. Both results are largely reproduced in our reanalysis. Comparing their Fig. 4 with the "default roughness" curve in Fig. 6.6 on p. 150, it appears that our result is slightly skewed towards lower thermal inertia. This may be due to the different fitting techniques used (Müller et al. do

not attempt to minimize χ^2 but rather the fractional formal diameter uncertainty, which is not entirely equivalent) and does not lead to significantly different results.

We conclude that the TPM by Lagerros (1996, 1997, 1998a) and that described herein are mutually consistent.

6.2.5 Summary

A TPM analysis of all available thermal-infrared data of the NEA (25143) Itokawa, the target of the Japanese mission Hayabusa, results in a diameter estimate between 320 and 330 m, in excellent agreement with the Hayabusa result of 327±6 m. Combining this with the results of our Eros study (see sect. 6.1) we conclude that 10 % is a conservative upper limit on the systematic diameter uncertainty inherent in our thermophysical modeling.

We find Itokawa's thermal inertia to be 700 ± 100 J s$^{-1/2}$K^{-1}m^{-2}, thus refining the estimate by Müller et al. (2005), which is based on a subset of the data available to us. A reanalysis of their database reproduces their results, thus demonstrating the mutual consistency of our TPM and that by Lagerros (1996, 1997, 1998a) which was used by Müller et al.

Itokawa's thermal inertia is intermediate between that of bare rock and dusty regolith. This is not straightforward to reconcile with Hayabusa close-up imaging results, which reveal a surface dominated by relatively large boulders. We speculate that boulders on Itokawa are covered with a thin coating of dust. This will be further discussed in sect. 7.3.3.c. We call for a reanalysis of the thermal-infrared database using the accurate Hayabusa-derived shape model, which has been released to the scientific community on 24 April 2007.

6.3 (1580) Betulia [8]

The C-type NEA (1580) Betulia is a highly unusual object for which earlier radiometric observations, interpreted on the basis of simple thermal models, indicated a surface of unusually high thermal inertia (see sect. 2.1).

We report results from extensive multi-wavelength thermal-infrared observations of Betulia obtained in 2002 with the NASA Infrared Telescope Facility IRTF.

---

[8] Most of the content of this section was prepublished (Harris et al., 2005a). I have reduced the presented data but have not contributed to planning and performing the observations. Two independent data analyses are presented in the paper, a NEATM analysis by the first author and a TPM analysis by myself. Only the latter analysis is presented here.

From a TPM analysis we determine that Betulia's thermal inertia is only moderate, around 180 J s$^{-1/2}$K^{-1}m^{-2}, comparable to our other NEA results. We determine an effective diameter of 4.57 ± 0.46 km and an albedo of $p_V = 0.077 \pm 0.015$, consistent with expectations based on the taxonomic type. Our results are in broad agreement with an independent NEATM analysis of the same data set but are hard to reconcile with previous results with indicate a much larger diameter and, indirectly, a high thermal inertia indicative of bare rock.

After publication, our diameter and albedo estimates have been confirmed on the basis of a reanalysis of available polarimetric data and, independently, on the basis of new radar observations.

6.3.1 Introduction

The C-type NEA (1580) Betulia is well known for its unusual lightcurve, the amplitude and form of which changes dramatically with changing solar phase angle; particularly, at large phase angles it exhibits a triply-peaked lightcurve as opposed to the doubly-peaked lightcurves of virtually all other asteroids (Tedesco et al., 1978). These and other lightcurve data were used by Kaasalainen et al. (2004b) to determine Betulia's spin state and a convex-definite model of its shape. They found the shape to be "very peculiar with a large planar area on one side" which they note may conceal a considerable concavity (their method of shape determination is designed to produce convex models). It is important to bear Betulia's unusual shape in mind when interpreting observational data with the aid of standard photometric, polarimetric, and radiometric techniques.

Betulia is also significant in being the first NEA for which thermal-infrared observations indicated a surface of high thermal inertia (see sect. 2.1). Lebofsky et al. (1978) obtained thermal-infrared data at a single thermal wavelength (10.6 µm). Using the STM (see sect. 2.4.1), which neglects thermal inertia, they obtained a diameter of 4.20 ± 0.80 km, inconsistent with a lower bound on the diameter of $D > 5.8 \pm 0.4$ km derived from radar observations (Pettengill et al., 1979) and furthermore with polarimetric observations, which appeared to indicate a diameter around 7 km (Tedesco et al., 1978). Because of this inconsistency, Lebofsky et al. rejected the STM diameter and used instead the FRM (see sect. 2.4.2), obtaining $D = 7.5 \pm 0.34$ km, concluding that Betulia had a very high thermal inertia, comparable to that of bare rock.

Betulia was observed extensively during an observing run with the NASA Infrared Telescope Facility (IRTF) in June 2002. Good quality data over a significant

Table 6.4: Betulia: Observing geometry. Values for the subsolar and sub-Earth latitude are based on the spin axis by Kaasalainen et al. (2004b).

	2002 June 02	2002 June 05
Heliocentric distance, r (AU)	1.143	1.150
Geocentric distance, Δ (AU)	0.246	0.263
Solar phase angle, α (°)	52.9	53.3
Subsolar latitude (°)	13	15
Sub-Earth latitude (°)	-39	-34

part of the rotation period were obtained at five wavelengths in the range 7–20 µm. We have fitted the resulting flux data with the TPM for convex shapes (see chapter 3) based on the shape model by Kaasalainen et al. (2004b).

6.3.2 Observations and data reduction

The observations were performed on 2002 June 2 and June 5 UT with the IRTF and JPL's 128×128 pixel, 7–25 µm infrared astronomical camera, MIRLIN. For details of MIRLIN see Ressler et al. (1994) and `http://cougar.jpl.nasa.gov/mirlin.html`. Measurements were made in N-band filters centered at (bandwidth in brackets): 7.91 (0.76), 10.27 (1.01), and 11.7 (1.11) µm, and in Q-band filters at: 17.93 (0.45) and 20.81 (1.65) µm. See Harris et al. (2005a) for details on the observations.

Standard synthetic aperture procedures (see sect. 4.4) were used for the derivation of raw signal counts from the MIRLIN images. Absolutely calibrated fluxes for the target asteroids were obtained by multiplying the integrated absolute fluxes of the calibration stars by the ratios of the target/calibration star raw counts in each filter. Absolutely calibrated infrared spectra for the calibration stars, α Boo and α Hya, were taken from the database of Cohen et al. (1999). Color corrections for the different flux distributions of the calibration stars and asteroids in the narrow filter pass bands were found to be no more than a few percent (Delbo', 2004) and were not applied.

Table 6.4 lists the observing geometry. The resulting fluxes are listed in table 6.5. The quoted uncertainties in the flux measurements refer to the formal statistical uncertainties in the synthetic aperture procedure, only. Errors in the absolute calibration and fluctuations in atmospheric conditions during the observations increase the scatter in the flux data. On 2002 June 2, an R-band (visible) lightcurve was obtained simultaneously with our IRTF observations on the Uni-

Table 6.5: Betulia: Measured flux values

| Date (UT)	Time (UT)	Julian date (days-2,452,420)	Wavelength (µm)	Flux (mJy)	Error (mJy)
2002-06-02	05:59	7.7493	7.91	1400	57
	07:03	7.7937	7.91	1789	61
	08:09	7.8396	7.91	1803	67
	06:07	7.7549	10.27	2270	36
	07:11	7.7993	10.27	3334	32
	08:17	7.8451	10.27	3315	45
	06:16	7.7611	11.70	2347	38
	07:19	7.8049	11.70	3900	36
	08:24	7.8500	11.70	3166	37
	06:29	7.7701	17.93	4445	568
	07:33	7.8146	17.93	4745	311
	08:37	7.8590	17.93	4670	343
2002-06-05	05:50	10.7431	7.91	1150	67
	07:04	10.7944	7.91	1277	74
	08:13	10.8424	7.91	1302	84
	05:57	10.7479	10.27	2171	60
	07:11	10.7993	10.27	2364	74
	08:20	10.8472	10.27	1998	71
	06:02	10.7514	11.70	2606	38
	07:16	10.8028	11.70	2312	51
	08:25	10.8507	11.70	2458	39
	06:13	10.7590	17.93	2635	247
	07:25	10.8090	17.93	3406	247
	08:35	10.8576	17.93	2528	290
	06:28	10.7694	20.81	3235	177
	07:39	10.8187	20.81	2663	189
	08:47	10.8660	20.81	3172	176
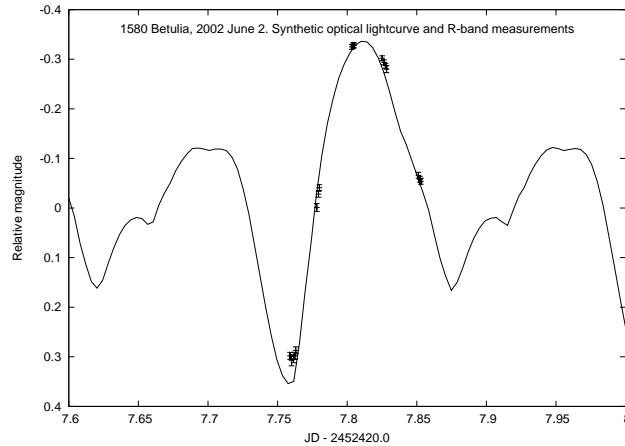
Figure 6.8: Betulia: Synthetic optical lightcurve using the shape model from Kaasalainen et al. (2004b) for the observing geometry of 2002 June 2. There is very good agreement in shape and amplitude between the synthetic curve and the corresponding R-band measurements. The positioning of the synthetic lightcurve relative to the R-band measurements was adjusted manually on both axes to obtain a good fit, leading to a slight correction to the rotational period within the uncertainties quoted by Kaasalainen et al. (see text for details).

versity of Hawaii's 88-inch telescope and kindly made available by Yan Fernández (2002, private communication).

6.3.3 Results

Our TPM analysis is based on the convex shape model by Kaasalainen et al. (2004b) which consists of 3192 triangular facets. The corresponding spin axis is $\beta = 21.92211922°$ and $\lambda = 133.275794°$ (J2000 ecliptic latitude and longitude, respectively; from M. Kaasalainen, 2003, private communication). Kaasalainen et al. (2004b) give a rotation period of 6.13836 ± 0.00001 h on the basis of observations between the years 1976 and 1989. Using these parameters, we have generated a synthetic optical lightcurve for the observing geometry of 2002 June 2 and compared it to the R-band data by Fernández (see Fig. 6.8). We found a slight offset in rotational phase of around 29 min which was corrected for by adjusting the rotation period to a value of 6.1383602 h, well within the quoted range of uncertainty.

Applying our TPM (see chapter 3) to the IRTF measurements listed in table 6.5, assuming $H = 15.1$ and $G = 0.15$ (see Harris et al., 2005a, and references therein), resulted in an effective diameter, D_{eff}, of 4.57 ± 0.15 km, a geometric albedo, p_{V}, of 0.077 ± 0.005, and a thermal inertia of 180 ± 50 J s$^{-1/2}$K^{-1}m^{-2}. The quoted errors
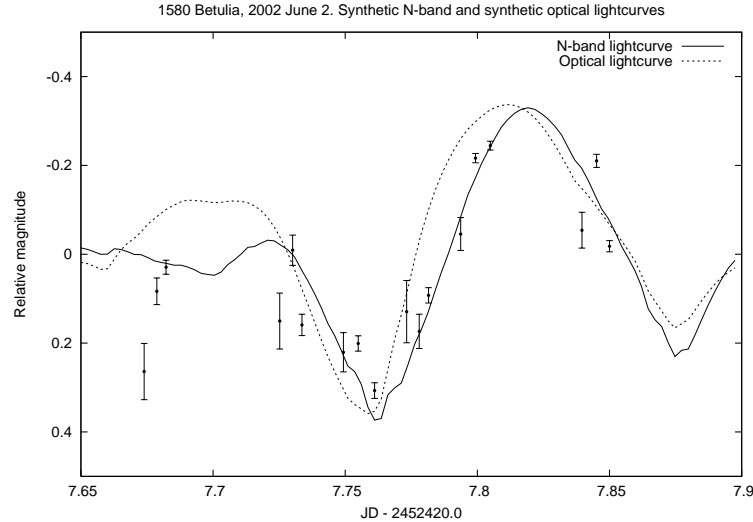
Figure 6.9: Betulia: Comparison of synthetic N-band and synthetic optical lightcurves for the observing geometry of 2002 June 2. Points corresponding to the measured N-band fluxes are superimposed. For this plot, data obtained on June 5 are referred to June 2 by subtracting 12 rotational periods and by adjusting the flux values for the changes in observing geometry (whereby the dominant effect is due to the change in geocentric distance, see table 6.4). No manual adjustments to the N-band synthetic lightcurve or measurement points were made.

reflect only the statistical scatter about the model curve; modeling uncertainties are much larger than the formal errors. Comparison with independent results for D_{eff} in the cases of (433) Eros and (25143) Itokawa suggests the uncertainty in diameter determinations with the TPM does not exceed 10 % (see sect. 7.2).

There is evidence in Fig. 6.9 for a phase lag between the observed optical and thermal-infrared lightcurves which has the same sense and appears to be roughly the same fraction of the rotation period as that observed by Lebofsky and Rieke (1979) in the case of (433) Eros, which they explained in terms of surface thermal inertia (see also sect. 6.1). Given the differences in the structure of the optical and N-band synthetic lightcurves evident in a comparison of the two lightcurves over a full rotation period, the significance of the apparent small phase lag is not clear. The synthetic Q-band lightcurve (Fig. 6.10) does not display a clear phase lag. The resolution of this discrepancy may lie in shortcomings of the shape model and the TPM: for example, possible variations in albedo and thermal inertia over the surface are ignored, and treatment of the surface structure in the TPM is limited to an idealistic distribution of hemispherical craters. We have no satisfactory quantitative explanation for the discrepancy at present and further development
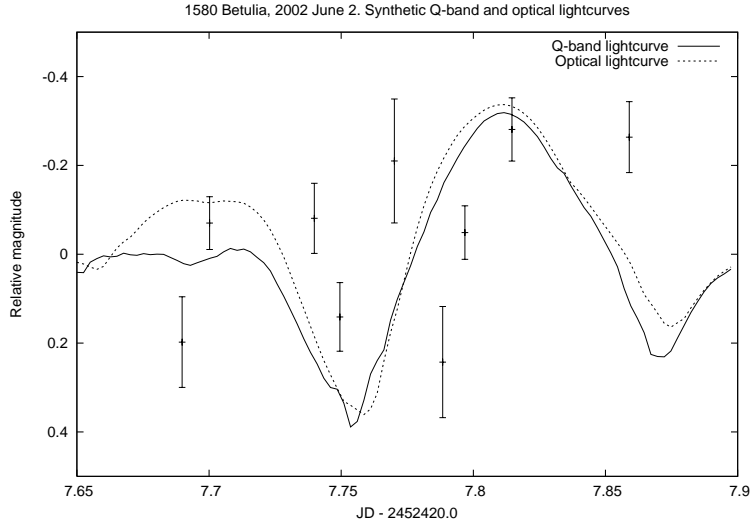
Figure 6.10: Betulia: Comparison of synthetic Q-band and synthetic optical lightcurves, points corresponding to the measured Q-band fluxes are superimposed as in Fig. 6.9. The plotted Q-band lightcurve results from parameters which best fit the total data set including N-band data.

of the model may be required to more accurately reproduce the details of the observations.

6.3.4 Discussion

Diameter and albedo   See table 6.6 for a comparison of our diameter and albedo result with previous determinations. It is instructive to first compare our results with the NEATM results by Harris et al. (2005a), which are based on the same

Table 6.6: Betulia: Summary of diameter and albedo determinations. Values given in brackets were determined by us, assuming $H = 15.1$, in order to facilitate comparison.

Source	D_{eff} (km)	p_{V}
This work	4.57 ± 0.46	0.077 ± 0.015
Tedesco et al. (1978), polarimetry	~ 7	~ 0.033
Lebofsky et al. (1978), STM	4.20 ± 0.80	(0.091 ± 0.035)
”, FRM	7.48 ± 0.34	(0.029 ± 0.003)
Pettengill et al. (1979), radar	> 5.4	(< 0.055)
Harris et al. (2005a), NEATM	3.82 ± 0.58	0.11 ± 0.04
Tedesco (2005, private communication)	4.76 ± 0.74	0.071 ± 0.005
Magri et al. (2007), radar	5.39 ± 0.54	(0.055 ± 0.011)

data set. While the TPM gives a somewhat larger diameter and lower albedo (the latter being more in line with expectations for a C-type asteroid) the two sets of results are in reasonable agreement given the uncertainties associated with both models, especially at the large solar phase angle at which our observations were made.

Our results are, however, inconsistent with the radar-derived lower limit on diameter of 5.8 ± 0.4 km (Pettengill et al., 1979) and with the polarimetric albedo result by Tedesco et al. (1978). Based on thermal-infrared observations at a single thermal wavelength (10.6 µm), Lebofsky et al. (1978) obtained two model-dependent diameter values, based on the STM (which neglects thermal inertia, see sect. 2.4.1) and the FRM (which effectively assumes infinite thermal inertia, see sect. 2.4.2), respectively. Our results are in good agreement with his STM result and inconsistent with his FRM result. Lebofsky et al. (1978), however, rejected the STM diameter in favor of the FRM result due to the better consistency of the latter with the results of Tedesco et al. (1978) and Pettengill et al. (1979). Betulia was the first asteroid for which the STM appeared to produce inconsistent results.

After the publication of our results, E. Tedesco (2005, private communication) has reanalyzed his published polarimetric data using a more recent calibration scheme, leading to a revised albedo estimate of $p_V = 0.071 \pm 0.005$. Together with the H value given in Harris et al. (2005a), $H = 15.1 \pm 0.3$, this implies $D = 4.76 \pm 0.74$ km in excellent agreement with our result.

Magri et al. (2007) report new radar observations of Betulia from which they determine an effective diameter of 5.39 ± 0.54 km, some 15 % larger than our result but within the combined ranges of uncertainty (see also sect. 7.2), and significantly below 7 km.

Shape From their radar observations combined with optical lightcurve data available in the literature, Magri et al. (2007) determined a new model of Betulia's shape. They confirm the spin-state estimate by Kaasalainen et al. (2004b) and largely confirm their convex-definite shape model. The radar shape model does, however, contain a few concavities including a very large concavity with a diameter comparable to Betulia's radius. The location of the latter is quoted to coincide with the large planar area in the Kaasalainen et al. model, where a concavity had been suggested by Kaasalainen et al.

We call for a reanalysis of our data based on the new radar shape model. At

the phase angles at which our observations took place (52.9 and 53.3°), shadowing inside the large concavity would be expected to lead to lower thermal fluxes relative to model fluxes for a convex shape, and might thus have caused us to underestimate the diameter. Depending on rotational phase, the concavity may or may not be oriented towards the observer, so it should produce an observable difference in the shape of the thermal lightcurve. Indeed, judging from Figures 6.9 (on p. 160) and 6.10, there appears to be a flux drop in both the N and the Q band at times shortward of 7.7, which is not reproduced by our TPM based on the convex shape model. Unfortunately, no optical lightcurve data are available for that time, so observational artefacts cannot be ruled out at the present time. The concavity is situated "on the southern hemisphere" (Magri et al., 2007) which was visible during our observations (see table 6.4 on p. 157).

Thermal inertia We obtain the first quantitative estimate of Betulia's thermal inertia, 180 ± 50 J s$^{-1/2}$K^{-1}m^{-2}, some three times larger than lunar regolith but an order of magnitude below bare rock (see table 3.1 on p. 58). We therefore find no evidence for a bare-rock surface of Betulia, in contrast with the suggestion by Lebofsky et al. (1978). We wish to emphasize that the thermal data at their disposal were taken at a single thermal wavelength and hence did not allow direct conclusions to be drawn on thermal properties (see also Fig. 2.1 on p. 27). In the light of the revised diameter estimates (see above) their reason to reject the STM diameter in favor of the FRM result no longer applies. In fact, their STM diameter is in good agreement with our result, providing indirect support for our moderate-thermal-inertia result.

Our thermal-inertia result is consistent with NEATM fits to our data set by Harris et al. (2005a), which resulted in $\eta = 1.09$, a value consistent with the presence of some thermally insulating regolith (see Delbo' et al., 2003).

In particular, our thermal-inertia result for Betulia is in line with our other thermal-inertia results for NEAs as discussed in sect. 7.3, while a very large thermal inertia as suggested by Lebofsky et al. would be unusual.

6.3.5 Summary

From a TPM analysis of thermal-infrared flux measurements of the NEA (1580) Betulia obtained at the NASA IRTF, we obtain a diameter of 4.57 ± 0.46 km, an albedo of $p_V = 0.077 \pm 0.015$, and a surface thermal inertia of 180 ± 50 J s$^{-1/2}$K^{-1}m^{-2}, or some three times the lunar value. This value of thermal inertia is less than 10 %

of that expected for a bare-rock surface and implies that the surface of Betulia has a significant thermally insulating regolith, in contrast to the conclusions of earlier work but consistent with our other thermal-inertia results for NEAs (see sect. 7.3).

Our results for diameter and albedo are in broad agreement with a NEATM analysis of the same data set (Harris et al., 2005a). The corresponding value of the model parameter, $\eta = 1.09$, is consistent with the presence of thermally insulating regolith. The difference between the results from the TPM and the NEATM is probably due to the complex shape and nature of Betulia and the more sophisticated treatment of the TPM, although we caution that neither model has been thoroughly tested at the high solar phase angles at which the IRTF observations were made.

Our diameter and albedo results are inconsistent with previous estimates based on polarimetric and radar data. After publication, however, our results were confirmed through a reanalysis of available polarimetric data based on up-to-date calibration schemes (Tedesco, 2005, private communication) and, independently, by Magri et al. (2007) based on new radar observations.

6.4 (54509) YORP [9]

We present preliminary results of Spitzer observations of the small NEA (54509) YORP (known until 2 April 2007 as 2000 PH5), which has an ultra-fast rotation period of only 12 minutes. Its rotation period has recently (Lowry et al., 2007; Taylor et al., 2007, published on-line on 8 March) been demonstrated to be steadily decreasing due to the YORP effect (see sect. 1.3) after which it has been named; together with the work by Kaasalainen et al. (2007) this constitutes the first direct detection of the YORP effect.

Further interest in (54509) YORP stems from the fact that it would be expected to be regolith-free due to its fast rotation: For any plausible mass density, gravity is overwhelmed by the centrifugal force on most of its surface.

Using the Spitzer Space Telescope we have obtained thermal lightcurves of (54509) YORP at wavelengths of 8, 16, and 22 µm with a time resolution of 14 s or better. From these, we obtain the diameter and thermal inertia of the asteroid.

The Spitzer Science Center has recently issued an updated calibration scheme

---

[9] A preliminary version of the results presented herein was presented in a poster at the IAU General Assembly 2006 in Prague.

which applies to two of our three data sets and is expected to lead to significant flux changes (see sect. 5.3.2.e). All results presented herein are based on the superseded calibration scheme and are therefore preliminary.

6.4.1 Introduction

The NEA (54509) YORP was discovered on 3 August 2000 by the MIT Lincoln Laboratory's near-Earth asteroid search program (LINEAR; Stokes et al., 2000). It is approximately co-orbital with Earth on a horseshoe orbit (see, e.g., Taylor et al., 2007, Fig. S1 in the supporting on-line material) and has undergone annual very close approaches with Earth in the years 2000–2005. It was soon found to be an ultra-fast rotator, with a period of only 12.17 min.

From extensive optical photometric observations in the years 2001–2005, Lowry et al. (2007) determined a steady linear increase in the angular velocity ω of $d\omega/dt = 2.0(\pm0.2) \times 10^{-4}$ deg day^{-2}. From radar observations obtained in the years 2001–2005 combined with the optical data by Lowry et al., Taylor et al. (2007) determined the spin state, shape, and diameter of YORP. They used their results as input parameters for model calculations of the change in spin rate expected from the YORP effect (see also sect. 1.3) and concluded that they have detected the latter. Together with Kaasalainen et al. (2007), who independently detected the YORP effect on another NEA, this constitutes the first direct detection of the YORP effect. Taylor et al. determined the J2000 ecliptic coordinates of the spin axis of YORP to be $\lambda = 180°$, $\beta = -85°$; a highly irregular shape; and a volume-equivalent diameter around 114 m. No formal diameter uncertainty is reported, in the following we assume a fractional uncertainty of 10 % as is usually reported for radar-derived diameters. Together with the absolute optical magnitude of $H = 22.562$ (NeoDys as of 11 May 2007), this diameter implies an albedo of $p_V = 0.13$.

Gietzen and Lacy (2007) report results of near-infrared spectroscopic observations of YORP. While a large amount of noise is apparent in their YORP data they report a clear detection of silicate features at 1 µm and 2 µm. They conclude that YORP belongs to either of the silicaceous taxonomic classes S or V. An S-type classification would suggest a moderate albedo around $p_V = 0.2$ (see, e.g., sect. 1.5.2), a much larger albedo would be associated with a V-type classification.

So far, no asteroid has been unambiguously shown to display a high thermal inertia indicative of a bare-rock surface. Fast rotators such as YORP are widely expected to be regolith-free bare rock (see, e.g. Whiteley et al., 2002) mainly

because their surface gravity cannot match the centrifugal force on most of their surface for reasonable values of mass density.

We have observed YORP with the Spitzer Space Telescope (see chapter 5) at three thermal wavelengths (8, 16, and 22 µm) in order to determine its size and thermal inertia. At each wavelength we have sampled the thermal lightcurve at a time resolution of 14 s or better. We have used our TPM described in chapter 3 to fit the data, based on a preliminary version of the shape model described in Taylor et al. (2007), which was kindly made available to us in computer-readable form by P. Taylor in 2006.

6.4.2 Spitzer observations

Our Spitzer observations have used the InfraRed Array Camera (IRAC, see sect. 5.2) for the 8 µm data and the InfraRed Spectrograph IRS in peak-up-imaging mode (PUI, see sect. 5.3.2) for observations at central wavelengths of ~ 16 and ~ 22 µm. Due to the design of IRAC, the asteroid was simultaneously observed at an effective wavelength of 4.5 µm; as expected, the asteroid signal in those "serendipitous" data is too noisy to be used. Our IRAC observations started on 18 August 2005, 17:50 UT, our PUI observations on 17 August 2005, 12:33 UT. The heliocentric distance at that epoch was 1.09 AU, the distance to Spitzer was 0.146 AU for the IRAC observations and 0.147 AU for the PUI observations, the solar phase angle was 59.3° for both. Assuming the spin axis given by Taylor et al. (2007), the aspect was nearly equatorial, with a subsolar latitude of 5° and sub-observer latitude of 13° at the epoch of the IRAC observations. The local time at the sub-observer point was 8.2 h, i.e. the cold "morning" side was observed (determined from the projections of the vectors towards the Sun and Spitzer onto the asteroid equator).

In order to obtain the finest possible time resolution, our observations were not dithered but used "in-place repeats" (see sect. 5.1.4 for a discussion of these observing modi). IRAC was pointed onto the asteroid (channels 2 and 4, at wavelengths of 4.5 and 8 µm, were simultaneously on target) for 60 consecutive exposures with frame times of 12 s each. Including short "dead" times between consecutive frames for, e.g., detector readout, the last exposure ended 13.6 min after the beginning of the first exposure, corresponding to 1.12 rotation periods and a time resolution of 13.6 s. With PUI, the asteroid was observed 55 times with PUI "blue" (effective filter wavelength ~ 22 µm), then 55 times with PUI "red" (effective filter wavelength ~ 16 µm). Each PUI frame had an integration time of

6 s; including "dead" times between consecutive frames, each series of 55 frames lasted 12.78 min corresponding to 1.05 rotation periods and a time resolution of 13.9 s. We expected the first few IRAC frames to be unusable due to the first-frame effect (see sect. 5.2.3.b), hence the slightly larger overlap between the two consecutive periods.

As recommended by the Spitzer Science Center (SSC), we did not perform dedicated calibration observations but relied on the calibration provided by the SSC, i.e. we started our data-reduction efforts at the level of Basic Calibrated Data (BCD) frames provided by the SSC (see also sect. 5.1.5). BCD frames are flux-calibrated images with most detector-specific artefacts removed. Note that the BCD pipeline for the PUI data has been updated on 28 February 2007; the PUI fluxes reported herein are based on the superseded pipeline version, significant calibration changes are to be expected from the new pipeline version (see also sect. 5.3.2.e).

Because our observations of YORP were not dithered we used a non-standard version of our data reduction pipeline. In particular, MOPEX could not be used for the automated rejection of outlier pixels such as cosmic ray hits. Instead, all BCD frames were visually inspected and rejected if obvious outliers were found within the vicinity of the target. The target was found to be clearly visible and well centered in all frames for wavelengths of 8, 16, and 22 µm. The serendipitous IRAC 4.5 µm observations of an identical field showed stellar background sources much more clearly than the simultaneous 8 µm frames. We additionally rejected IRAC 8 µm frames when the corresponding 4.5 µm frame displayed significant background structure close to the center, i.e. the asteroid position (which was discernible in some 4.5 µm frames). No background sources were found in the PUI frames.

The remaining IRAC frames were in a first step reprojected onto a rectangular grid to correct them for optical distortion, using MOPEX (see sect. 5.2.4.c). Then, they were converted from flux units of MJy/sr into units of mJy/pixel using a dedicated IDL routine. On the resulting frames, synthetic aperture photometry was performed (see sect. 5.2.4.e) for different aperture radii. The resulting flux values were aperture corrected to account for flux losses due to the limited radius of the synthetic apertures (see sect. 5.2.4.f). Flux uncertainties were estimated from the statistical scatter of the individual flux vales (for any particular aperture radius) and the scatter in the flux set for all aperture radii; the uncertainty contributions were added in quadrature (see sect. 5.2.4.h). Analogous procedures were used for
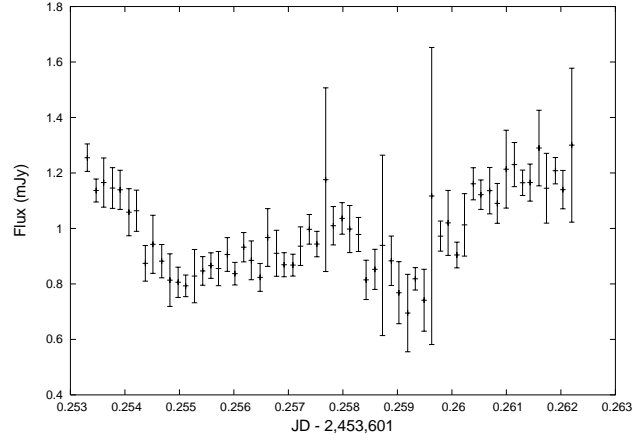
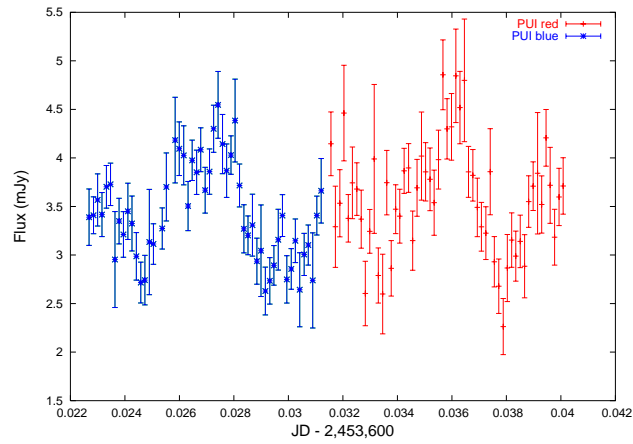**Figure 6.11:** Plot of IRAC-channel-4 fluxes obtained for YORP.

Figure 6.12: Plot of PUI fluxes obtained for YORP.

PUI frames.

Final fluxes for each wavelength were averaged and fitted using the NEATM. Color-correction factors (see sect. 5.2.4.g and 5.3.2.d) were determined for the resulting NEATM model parameters. This procedure was reiterated using the color-corrected fluxes as NEATM input until stable color-correction factors have been obtained (after the second iteration).

For each observation, the time of mid-exposure was determined and one-way lighttime was subtracted. Given the Spitzer-centric distance of ~ 0.05 AU, lighttime was ~ 0.4 min, or $\sim 12°$ in rotational phase.

See Fig. 6.11 for the resulting IRAC fluxes and Fig. 6.12 for the resulting PUI fluxes. There are some data points with much larger flux uncertainties than the
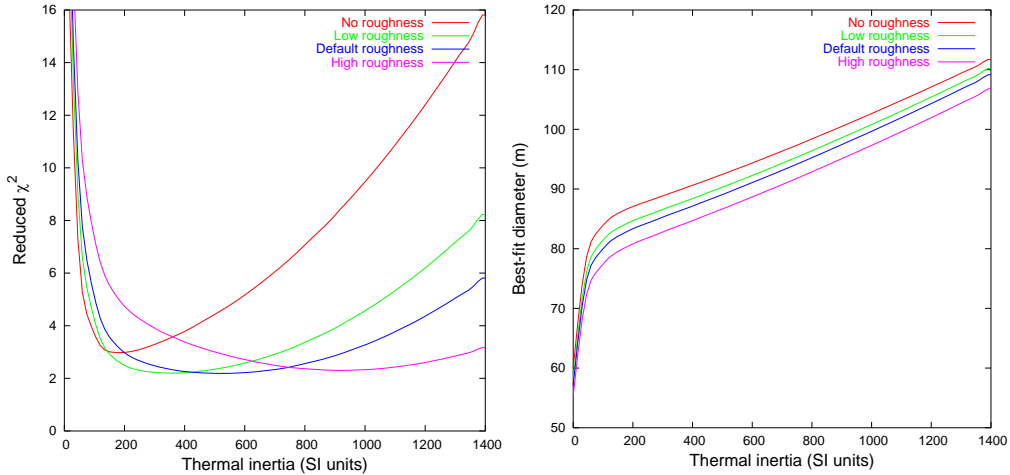
Figure 6.13: TPM fits to our Spitzer data of YORP: reduced χ^2 (left) and best-fit diameter (right) as a function of thermal inertia for different sets of roughness parameters.

others. It has been verified for a few of them that there are slight image artefacts close to the source which have not been caught during first visual inspection. They were kept in the database to avoid the introduction of subjective bias; due to their large error bars those fluxes are given duly low weight in the fitting process. As detailed in chapter 5, the effective wavelengths are 7.872, 15.7929, and 22.3272 µm.

6.4.3 Results

We used our TPM described in chapter 3 together with a preliminary version of the the shape model reported by Taylor et al. (2007) for YORP to fit the resulting flux values. The reported value for the angular acceleration caused by the YORP effect was used in the determination of rotational phases for a given epoch, no manual adjustment of rotational phase has been made. See Fig. 6.13 for the results (see sect. 6.1 for a detailed discussion of analogous plots). As apparent in the left figure, there are different χ^2 minima depending on the roughness parameters used. While zero roughness appears to be less consistent with the data than non-zero roughness, the remaining three roughness models appear to fit the data equally well. Thermal-inertia values in the range 200–1200 J s$^{-1/2}$K^{-1}m^{-2} are consistent with the data. The corresponding range in best-fit diameter is 88–96 m, corresponding to a geometric albedo p_V between 0.18 and 0.22.

Synthetic model lightcurves for different parameters have been superimposed on two of our three data sets (see Fig. 6.14). A similar plot for the third data set would look qualitatively identical.
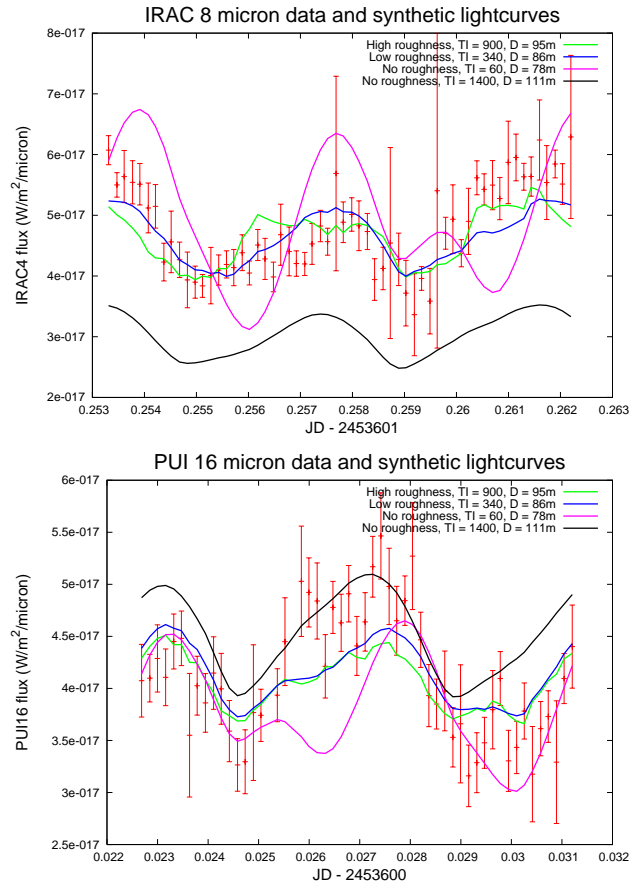
Figure 6.14: IRAC data as shown in Fig. 6.11 and "blue" PUI data as shown in Fig. 6.12 superimposed on four synthetic lightcurves. In both plots, the green and blue lines correspond to best-fitting parameters for different roughness models (cf. Fig. 6.13). The lines in magenta and black illustrate the effect of very low and very high thermal inertia: Low thermal inertia leads to large lightcurve amplitudes; high thermal inertia smoothes the lightcurve shape and amplitude. Furthermore, thermal inertia influences the ratio of flux levels at different wavelengths (color temperature); clearly, the black lines poorly fit the color temperature.

6.4.4 Discussion

6.4.4.a Fit quality

As apparent in Fig. 6.14, our TPM based on the preliminary shape model by Taylor et al. (2007) provides a reasonably good fit to our Spitzer data. It is clearly seen that very large and very low values of thermal inertia can be ruled out on the basis of the resulting lightcurve shape.

We wish to emphasize that no manual adjustment was made to the rotational phase determined from the shape model and the Spitzer-centric observing geometry at the time of observation. The good phase agreement between our Spitzer data and the synthetic lightcurves provides further evidence for the validity of the spin up of YORP due to the YORP effect (see Taylor et al., 2007, note 23).

We also note that some lightcurve features are not adequately reproduced (e.g. that around a time of 0.026 in the 16 μm lightcurve). This may be due to the fact that we use the convex-shape TPM although the shape model by Taylor et al. (2007) is not convex. At the time of writing, the concave-shape TPM described in chapter A is not yet sufficiently well tested and stable to be used for this purpose. We also note that we do not yet have the final shape model by Taylor et al. at our disposal. Our results are therefore preliminary.

6.4.4.b Diameter and albedo

Assuming a systematic modeling uncertainty in diameter of 10 % (see sect. 7.2), the range in diameter that best fits our data is 92 ± 10 m, corresponding to $p_V = 0.20 \pm 0.04$. The true modeling uncertainty in this case may be larger due to the concavities present in the Taylor et al. shape model, which are currently neglected in our TPM. At the phase angle of our observations ($59.3°$), shadowing effects would reduce the amount of observable flux relative to our model calculations, hence we would expect our model to somewhat underestimate the diameter and, correspondingly, to overestimate p_V.

An additional source of uncertainty is the flux calibration of the PUI data sets which account for two thirds of our database; the new calibration pipeline recently issued by the Spitzer Science Center is reported to cause calibration changes of up to 15 %. If our diameter result were entirely based on PUI fluxes, the corresponding change in diameter would be up to 7.5 %.

Taken together, our preliminary diameter result appears not to be inconsistent with the radar-derived diameter of 114 ± 12 m by Taylor et al. (2007), where

we assume a fractional diameter uncertainty of 10 % as is usually reported for radar-derived diameters (no diameter uncertainty is reported by Taylor et al.).

From spectroscopic observations, Gietzen and Lacy (2007) conclude that YORP belongs to either of the taxonomic classes S or V. S-type classification would indicate an albedo of $p_{\rm V} \sim 0.2$, a much larger value would be expected for V types. An S-type classification would be in excellent agreement with our albedo result and would not be inconsistent with that implied by the radar diameter ($p_{\rm V} = 0.13 \pm 0.03$). A V-type classification would appear to be inconsistent with both diameter determinations.

6.4.4.c Thermal inertia

Unfortunately, the thermal inertia of YORP is not well constrained by our preliminary data analysis, although a low thermal inertia comparable to the lunar value is clearly inconsistent with the data (see Fig. 6.13). Interestingly, also large thermal-inertia values close to that expected for bare rock (~ 2500 J s$^{-1/2}$K^{-1}m^{-2}) appear to be inconsistent, with 1200 J s$^{-1/2}$K^{-1}m^{-2} being a tentative upper limit. We wish to emphasize that these are only preliminary results and that a final analysis may well result in a higher thermal inertia.

6.4.5 Summary

Using the Spitzer Space Telescope, we have obtained thermal lightcurves of the ultra-fast rotating NEA (54509) YORP at wavelengths of 8, 16, and 22 µm. A preliminary data analysis demonstrates the potential of our TPM to constrain the thermal properties of this $D \sim 100$ m object. As expected, a very low thermal inertia indicative of a thick dusty regolith is clearly excluded by our data, while we cannot confirm our expectation, namely a large thermal inertia indicative of bare rock. Rather, an intermediate range between some 200 and 1200 J s$^{-1/2}$K^{-1}m^{-2} appears to best fit the data. See sect. 7.3.3.c for a discussion. We caution that our result is preliminary due to uncertainties in the flux calibration.

6.5 (33342) 1998 WT24 [10]

The potentially hazardous asteroid (33342) 1998 WT24 approached the Earth within 0.0125 AU on 16 December 2001 and was the target of a number of optical, infrared, and radar observing campaigns. Interest in 1998 WT24 stems from its having an orbit with an unusually low perihelion distance, which causes it to cross the orbits of the Earth, Venus, and Mercury, and its possibly being a member of the E spectral class, which is rare amongst NEAs. We present a TPM analysis of an extensive database resulting from thermal-infrared observations of 1998 WT24 obtained in December 2001 with the 3-m NASA Infrared Telescope Facility (IRTF) on Mauna Kea, Hawai'i and the ESO 3.6-m telescope in Chile at large solar phase angles.

We have obtained best-fit values of 0.35 ± 0.04 km for the effective diameter, 0.56 ± 0.2 for the geometric albedo, p_V, and 100–300 J s$^{-1/2}$K^{-1}m^{-2} for the thermal inertia. Our results are in good agreement with independent analyses of the same data set. Our values for the diameter and albedo are consistent with results derived from radar and polarimetric observations. The albedo is one of the highest values obtained for any asteroid and, since no other taxonomic type is associated with albedos above 0.5, supports the suggested rare E-type classification for 1998 WT24. The thermal inertia is an order of magnitude higher than values derived for large main-belt asteroids but consistent with the relatively high values found for other near-Earth asteroids.

6.5.1 Introduction

(33342) 1998 WT24 was discovered on 1998 November 25 by the LINEAR (Stokes et al., 2000) search program. Observations of physical characteristics published to date suggest that 1998 WT24 is a rare E-type Aten NEA with a high polarimetric albedo of around 0.43 (Lazzarin et al., 2004b; Kiselev et al., 2002). The E class is the taxonomic class which is associated with the highest albedo values, typically in the range $p_V = 0.3$–0.6 (see also sect. 1.5.2). Examples of main-belt E-types are (44) Nysa (IRAS $p_V = 0.55$, Tedesco et al., 2002a) and (64) Angelina ($p_V = 0.40$, Tedesco et al., 2002b). Only four other E-type NEAs are known so far: (3103) Eger (Clark et al., 2004a; Gaffey et al., 1992), (10302) 1989 ML (see sect. 6.7),

---

[10] The content of this section was prepublished (Harris et al., 2007). I have not contributed to obtaining the data, but have performed a TPM analysis thereof (our TPM is referred to as "General Thermophysical Model" in the paper).

and (4660) Nereus and (5751) Zao (Delbo' et al., 2003).

For 1998 WT24, Krugly et al. (2002) report a rather short rotation period of 3.697 h and a lightcurve amplitude measured at solar phase angles between $50°$ and $60°$ of 0.26 mag. The absolute magnitude at maximum brightness derived by Kiselev et al. (2002) is 18.69 ± 0.08 mag, or 18.39 ± 0.08 mag if a brightness opposition effect is assumed similar to that observed for the E-type asteroids (44) Nysa and (64) Angelina. Given the reported 0.53 mag lightcurve amplitude at the time of the Kiselev et al. photometric observations (2001 December 2.9), the Kiselev et al. result of $H_{max} = 18.39 \pm 0.08$ mag is compatible with H (lightcurve mean) $= 18.54 \pm 0.1$ mag derived independently by Delbo' (2004) using the method of Bowell et al. (1989) on observations made at ESO on 2001 December 2 and 4, taking $G = 0.4$. Taking $H = 18.5 \pm 0.3$, the diameter of (33342) 1998 WT24 inferred from an albedo of $p_V = 0.43$ is $D = 0.40 \pm 0.06$ km. It should be noted, however, that the derivation of albedos from polarimetric observations is based on a method that depends on empirically derived relations between the polarization parameters and the solar phase angle and albedo and that different calibrations of this method have been published, most recently by Cellino et al. (1999). Kiselev et al. used the relations of Lupishko and Mohamed (1996). If we take the Kiselev et al. value of $h_v = 0.039 \%$ $\deg^{-1}$ for the slope of the linear part of the polarization-phase curve and apply the appropriate relation of Cellino et al. (1999), we find a higher albedo of $p_V = 0.62$. Assuming $H = 18.5 \pm 0.3$, the implied diameter is reduced to $D = 0.34 \pm 0.05$ km. Goldstone radar images of 1998 WT24 made available on the web by S. Ostro and colleagues (`http://neo.jpl.nasa.gov/images/1998wt24.html`) suggest a slightly elongated body with a possible concavity. However, no formal report of the Goldstone observations is available at the time of writing. Zaitsev et al. (2002) made radar observations of 1998 WT24 on 2001 December 16 and 17 and derived lower limits for the maximum pole-on breadth of the asteroid of $D_{max} = 0.42$ and 0.40 km, respectively, from observations of the Doppler-broadened echo bandwidth, B, on the two dates. B is proportional to $D_{max} \times \sin \psi$, where ψ is the angle between the spin vector and the radar line-of-sight. Since the pole orientation of 1998 WT24 is unknown, only a lower limit for the maximum pole-on dimension can be determined from the radar data.

No pole solution for 1998 WT24 has been published to date. However, clues concerning the pole direction can be derived by comparing diameter results from different sources. In particular, a comparison of the available polarimetric and

Table 6.7: 1998 WT24: observing geometry. Note: The sense of the solar phase angle changed on December 15. For example, if rotation is retrograde, the cooler morning side of the asteroid was observed prior to December 15 and the warmer afternoon side after December 15.

	2001 Dec. 4	2001 Dec. 18	2001 Dec. 19	2001 Dec. 21
Telescope	ESO	IRTF	IRTF	IRTF
Heliocentric distance, r (AU)	1.0148	0.9901	0.9874	0.9817
Geocentric distance, Δ (AU)	0.0621	0.0162	0.0198	0.0284
Solar phase angle, α (°)	-60.4	67.5	79.3	93.4

radar results suggests that the sub-Earth latitude at the time of the Zaitsev et al. radar observations was small (or, equivalently, that the angle ψ defined above was close to $90°$). Based on a simple-model analysis of the thermal-infrared data discussed herein, Harris et al. (2007) suggest that the subsolar latitude was close to zero during the time of their observations. Taken together, these two constraints lead to a crude estimate on the spin axis position with ecliptic latitude β and longitude λ close to $\beta = 52°$, $\lambda = 175°$ or $\beta = $ -52°, $\lambda = 355°$, depending on whether the rotation is prograde or retrograde, respectively, where "the quoted solutions may be in error by several tens of degrees." (Harris et al., 2007)

Thermal-infrared flux measurements were obtained at wavelengths in the range 7–21 µm. The observing nights were partially compromised by poor weather and instrument problems but the availability of independent data sets from four nights in total with a broad range of observing geometries (see table 6.7) has nevertheless enabled substantial, self-consistent results to be derived.

6.5.2 Data

(33342) 1998 WT24 was observed with the ESO 3.6-m telescope and the IRTF in December 2001. I have not contributed to obtaining these data, the flux values are quoted here for completeness; see Harris et al. (2007) for details on the observations and the data reduction.

Thermal fluxes are listed in table 6.8 on p. 176. The quoted uncertainties in the flux measurements refer to the formal statistical uncertainties in the synthetic aperture procedure, only. The data quality is variable due to fluctuating atmospheric and instrumental circumstances. In particular, the Dec. 18 observations were affected by partially non-photometric conditions and problems with the filter wheel. The scatter of multiple measurements made in the same filter (see, e.g., Harris et al., 2007, Fig. 1) reveals the presence of non-statistical variability in the

Table 6.8: 1998 WT24: measured fluxes, quoted after Harris et al. (2007).

Date (UT)	Time (UT)	Julian date (days-2,452,240)	Wavelength (µm)	Flux (mJy)	Error (mJy)
2001-12-04	09:10	7.8819	8.73	144	31
	08:53	7.8701	10.38	239	15
	08:50	7.8681	11.66	262	37
2001-12-18	05:32	21.7306	7.91	2859	246
	05:33	21.7312	7.91 3	109	265
	05:57	21.7479	10.27	5017	189
	05:58	21.7486	10.27	4226	161
	05:30	21.7292	11.70	4887	83
	05:38	21.7347	11.70	4592	121
	05:39	21.7354	11.70	5177	92
	05:55	21.7465	11.70	4880	91
	05:34	21.7319	17.93	5849	1219
	05:45	21.7396	17.93	7005	887
2001-12-19	05:48	22.7417	7.91	1758	62
	06:17	22.7618	7.91	1416	54
	06:49	22.7840	7.91	1444	66
	05:05	22.7118	11.70	3180	68
	05:51	22.7437	11.70	3220	48
	06:20	22.7639	11.70	3294	51
	06:52	22.7861	11.70	2658	63
	05:12	22.7167	17.93	3847	217
	05:57	22.7479	17.93	3402	230
	06:25	22.7674	17.93	3079	293
	06:59	22.7910	17.93	3805	382
	05:23	22.7243	20.81	4959	736
2001-12-21	04:53	24.7035	7.91	489	50
	05:48	24.7417	7.91	546	57
	05:01	24.7090	10.27	915	31
	05:55	24.7465	10.27	1058	45
	05:07	24.7132	11.70	1146	33
	06:01	24.7507	11.70	1384	49
	05:20	24.7222	17.93	1915	103
	06:14	24.7597	17.93	2119	202

data, which is probably due mainly to rotation of the asteroid and variable atmospheric conditions. However, our model fitting routines effectively take account of the scatter in multiple measurements, in addition to the statistical uncertainties, and weight the data accordingly, which mitigates against serious errors due to non-statistical variability.

6.5.3 Results

We have applied our TPM described in chapter 3 to the thermal-infrared data of 1998 WT24 given in table 6.8. Since no shape model has yet been published for 1998 WT24, we first tried modeling the asteroid as a biaxial ellipsoid spinning about one of the two shorter axes. The ellipsoid was modeled as a mesh of 6144 triangular facets. Several types of ellipsoid were tried, all of which were consistent with published optical lightcurves, but the results turned out to be largely independent of the shape of the ellipsoid. In fact, it was found that no ellipsoid fitted the thermal data significantly better than a sphere. Therefore, we pursued our analysis assuming a spherical shape.

For both possible spin directions (see sect. 6.5.1) surface roughness, thermal inertia, and size were adjusted until the best agreement was obtained with the full set of observational results listed in table 6.8, i.e. χ^2 was minimized. It was found that the fit significantly improved when the data from December 18 were excluded, which is consistent with these data being of inferior quality, as discussed in Harris et al. (2007). They are disregarded in the following.

We found the retrograde pole solution to fit the data significantly better than the prograde solution (see Fig. 6.15 on p. 178). For the retrograde pole solution, and different degrees of surface roughness (see sect. 3.5 for a discussion of the roughness parameters used), the best-fit thermal inertia is about 200 J s$^{-1/2}$K^{-1}m^{-2}, with an uncertainty of some 100 J s$^{-1/2}$K^{-1}m^{-2} (see Fig. 6.16). Zero roughness and the highest degree of roughness (saturated crater coverage) give slightly worse fits to the data. In the case of zero roughness we note that our TPM gives very similar results to those of the independently developed smooth-sphere model presented by Harris et al. (2007). The corresponding best-fit values of diameter and albedo are 0.35 ± 0.02 km (where the uncertainty solely reflects the flux scatter) and $p_V = 0.56 \pm 0.2$ (assuming $H = 18.5 \pm 0.3$). Fig. 6.17 illustrates the dependence of diameter on roughness and thermal inertia.

We note that a crucial TPM input parameter, namely the spin axis determined by Harris et al. (2007), is uncertain to within a few tens of degrees. To study
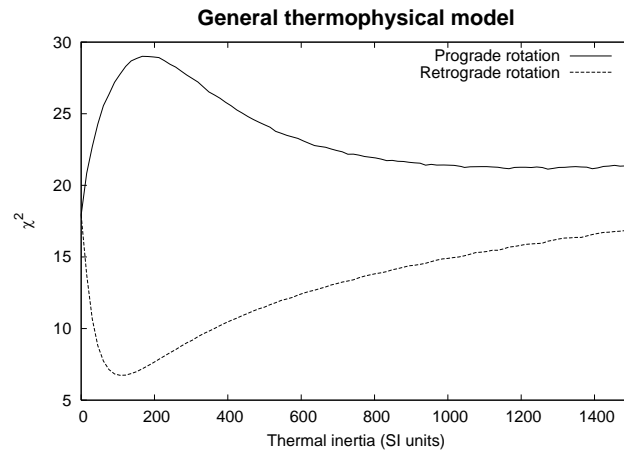
Figure 6.15: 1998 WT24: Goodness of fit (reduced χ^2) as a function of thermal inertia for the two possible spin axis orientations and a smooth surface. Adding surface roughness does not alter the clear preference for retrograde rotation. Note the convergence of the two curves as thermal inertia approaches zero, where the temperature distribution is no longer sensitive to the spin state.
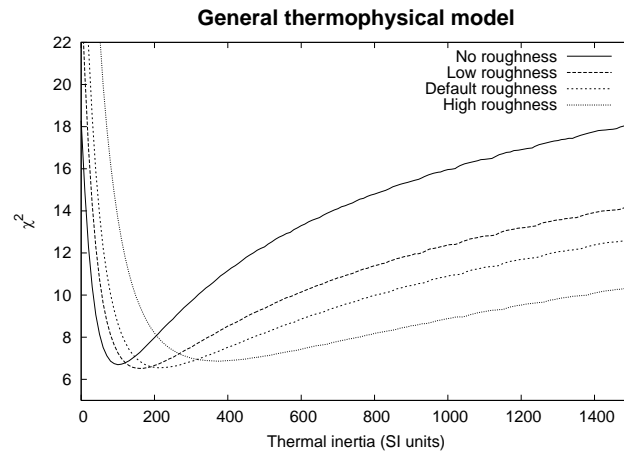
Figure 6.16: 1998 WT24: Goodness of fit (reduced χ^2) as a function of thermal inertia for retrograde rotation and different degrees of surface roughness.
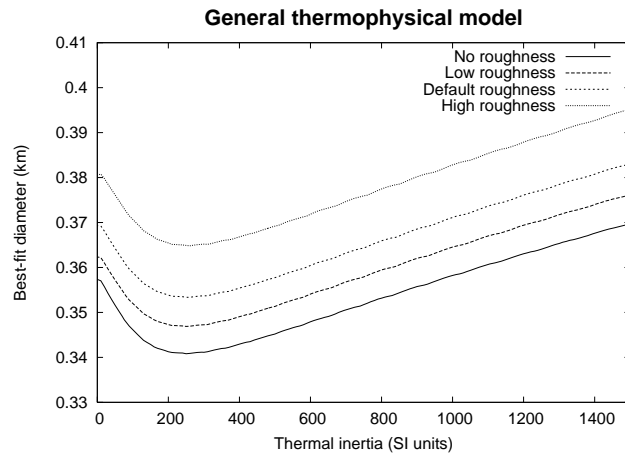
Figure 6.17: 1998 WT24: Dependence of best-fit diameter on thermal inertia for different degrees of surface roughness.
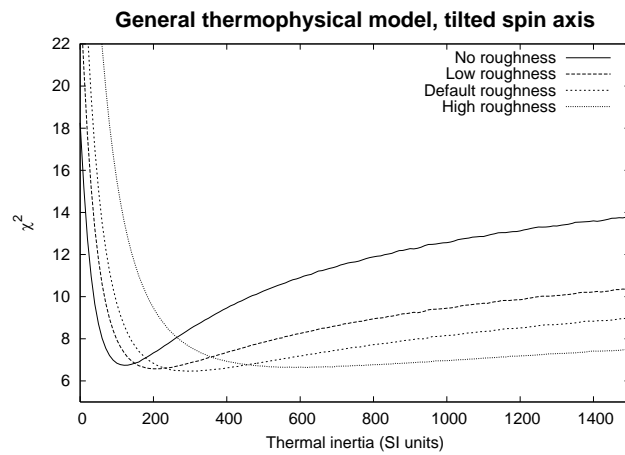

Figure 6.18: Like Fig. 6.16 but with a spin axis tilted towards the Sun by 30° relative to the nominal retrograde solution (for the ephemeris of the radar observations).
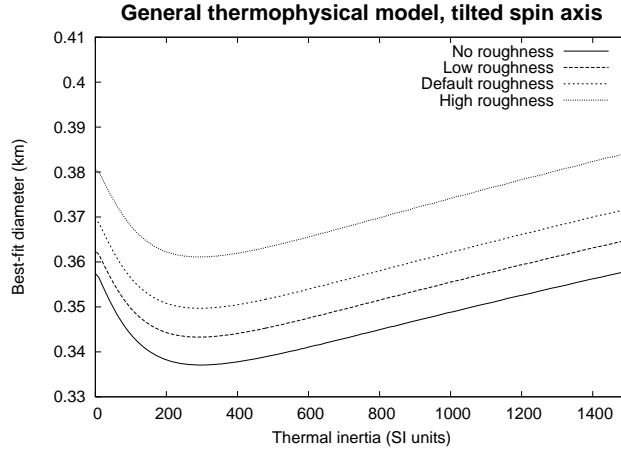
General thermophysical model, tilted spin axis

Figure 6.19: Like Fig. 6.17 but with a tilted spin axis as in Fig. 6.18.

the maximum possible effect thereof on our results, we have repeated our TPM analysis assuming a hypothetical spin axis position which is tilted towards the Sun (for the ephemeris of the radar observations by Zaitsev et al., 2002) by 30° relative to the nominal retrograde spin solution. We estimate that a tilt angle largely exceeding 30° would be inconsistent with the arguments presented by Harris et al. (2007). Tilting the axis towards the Sun rather than to the observer or into some random direction maximizes the effect on the model temperature distribution and hence on the resulting thermal-inertia estimate. In particular, the effect of thermal inertia on diurnal temperature curves is maximized for a subsolar latitude of zero and vanishes for a subsolar latitude of ±90°. At an increased subsolar latitude, therefore, the model would be expected to require a larger thermal-inertia value to match the observed data. Indeed, Fig. 6.18 displays χ^2-minima which are, compared to Fig. 6.16, slightly shifted towards larger thermal-inertia values for all choices of roughness parameters. Keeping in mind that this simulation is close to a worst-case scenario, we feel that in this case we can neglect the spin-axis-induced uncertainty in thermal inertia. The same applies to the resulting best-fit diameter (Fig. 6.19).

6.5.4 Discussion

The thermal-infrared data of 1998 WT24 considered here have been obtained at large phase angles exceeding 60°. At such large phase angles, unresolved topographic structure, such as large concavities or boulders, could significantly influence the temperature distribution on the surface, so we caution that the modeling

Table 6.9: Summary of diameter, albedo, and thermal inertia determinations for (33342) 1998 WT24. Values in brackets are calculated by us assuming $H = 18.5 \pm 0.3$.

D_{eff} (km)	p_{V}	Thermal inertia $(\mathrm{J\ s^{-1/2}K^{-1}m^{-2}})$	Source
(0.40 ± 0.13)	0.43 ± 0.15	—	Kiselev et al. (2002), (Lupishko and Mohamed, 1996, calibration)
(0.34 ± 0.10)	0.62 ± 0.17	—	Kiselev et al. (2002), (Cellino et al., 1999, calibration)
$D_{\mathrm{max}} > 0.40$	—	—	Zaitsev et al. (2002)
0.34 ± 0.02	0.60 ± 0.2	~ 100	Harris et al. (2007), "smooth-sphere TPM"
~ 0.36	~ 0.56	—	Harris et al. (2007), data from Dec. 21, FRM
< 0.41	> 0.42	—	Harris et al. (2007), data from Dec. 4, 19, NEATM
0.35 ± 0.02	0.56 ± 0.2	100–300	This work

uncertainties in our results are considerable, in particular since we do not have a physical shape model of 1998 WT24 at our disposal. Nevertheless, despite the fact that our TPM and all the thermal models used in analyses of the same data set (Harris et al., 2007) have their shortcomings and have not been thoroughly tested at the high phase angles of our 1998 WT24 observations, the overall agreement of the results from the various models is good (see table 6.9). We assume that the uncertainty in our diameter estimate is dominated by systematic modeling uncertainties, which we estimate to be 10 % at most (see sect. 7.2), so our conservative estimate of the diameter of 1998 WT24 is 0.35 ± 0.04 km.

Furthermore, our results agree with those by Kiselev et al. (2002), which are based on polarimetric observations. Zaitsev et al. (2002) derived lower limits for the maximum pole-on breadth of 0.42 and 0.40 km, respectively, from observations of the Doppler-broadened radar echo bandwidth on two consecutive dates. Zaitsev et al. interpret the constancy of their radar echo bandwidths as indicating a roughly spherical shape. The lightcurve amplitude of 0.26 mag peak to peak reported by Krugly et al. (2002) at phase angles between $50°$ and $60°$ suggests an axial ratio of roughly $a/b = 1.15$, after reducing the lightcurve amplitude by a factor of 1.7 to crudely correct for the phase-angle dependence (Zappalà et al., 1990). Given the effective diameter of 0.35 km derived in this work, the corresponding dimensions of a biaxial ellipsoid would be $a = 0.38$ km and $b = 0.33$ km. The larger dimension is consistent with the results of Zaitsev et al. (2002), given the uncertainties.

We conclude that our results are consistent with published values for the diameter and albedo derived using independent techniques (table 6.9), which increases our confidence in the thermal inertia derived in this work. Our thermal-inertia result is well in line with our other thermal-inertia results for NEAs.

Our albedo for 1998 WT24 of $p_V = 0.56 \pm 0.2$ is at the high end of the range associated with E types in general and means that this object has one of the highest albedos measured for any asteroid. The uncertainty in our derived albedo is, however, relatively large, due to modeling uncertainties and the uncertainty in the H value. A fainter H value would lead to a lower albedo but would have little influence on the derived diameter or thermal inertia.

6.5.5 Summary

Using our TPM to fit thermal-infrared flux measurements of the NEA 1998 WT24 results in an effective diameter of 0.35 ± 0.04 km and an albedo of $p_V = 0.56 \pm 0.2$ (the conservative uncertainties allow for modeling errors and, in the case of p_V, the uncertainty in H), and indicates that the surface thermal inertia is around 100–300 J s$^{-1/2}$K^{-1}m^{-2}, or a few times the lunar value. The high albedo is consistent with the suggestion that 1998 WT24 is a member of the E spectral class. The thermal inertia is much lower than that expected for a bare-rock surface and implies that 1998 WT24 has significant areas of thermally insulating regolith, consistent with our other thermal-inertia results for NEAs. Our results suggest that 1998 WT24 is a retrograde rotator. It has been verified that the uncertainty in the spin-axis position reported by Harris et al. (2007) induces a negligible uncertainty in thermal inertia, size, and albedo, relative to other sources of uncertainty.

Given the large solar phase angles, in excess of $60°$, at which the thermal-infrared observations took place, our diameter and albedo results are in remarkably good agreement with results of several other analyses of the same data set and furthermore with results from polarimetric and radar observations.

6.6 (21) Lutetia, Rosetta flyby target [11]

The ESA spacecraft Rosetta, which was launched in 2004 and is currently on its way to comet 67P/Tschurjumow-Gerasimenko, will fly by the main-belt asteroid (MBA) (21) Lutetia in 2010, at a planned flyby distance of about 3000 km and a relative velocity of 15 km/s. Lutetia is classified as an M type, but recent spectroscopic observations indicate a primitive, carbonaceous-chondrite-like (C-type) surface composition for which a low geometric albedo would be expected; this

---

[11] Most of this section was prepublished (Mueller et al., 2006). I have planned the observations, which were performed by co-author SJB. Data were analyzed by MM and AWH. The remaining three co-authors (JLH, MK, and JDA) represent the MIRSI team which built the mid-infrared imager used in the observations.

is incompatible with the IRAS albedo of 0.221±0.020. To assist the flyby planning, we have observed Lutetia using the IRTF. We infer that Lutetia has a diameter of 98.3 ± 5.9 km and a geometric albedo of 0.208 ± 0.025, in excellent agreement with the IRAS value and consistent with an M-type classification. We can thus rule out a low albedo typical of a C-type taxonomic classification. Furthermore, we find that Lutetia's thermal properties are well within the range expected for an asteroid of its size.

6.6.1 Introduction

During its journey to the comet 67P/Tschurjumow-Gerasimenko, the ESA space-craft Rosetta is scheduled to fly by two MBAs (Barucci et al., 2005): 2867 Šteins in September 2008 and 21 Lutetia in July 2010. Due to its small size of just a few kilometers, little is known about Šteins. On the other hand, Lutetia with a diameter of about 100 km is rather well observed at various wavelengths. However, the emerging picture of its surface composition is ambiguous: Based on color measurements and the IRAS albedo of 0.221 ± 0.020, Tholen (1989) classified Lutetia as M type, therefore it was generally believed to have a metallic surface composition. Howell et al. (1994) confirm this classification using a larger data set (they noted that Lutetia has an affinity to the C-class but ruled it out on the basis of the IRAS albedo). Based on CCD spectroscopy, Bus and Binzel (2002) classified Lutetia as X_k-type, which is compatible with a metallic surface composition. However, in recent work by Birlan et al. (2004); Lazzarin et al. (2004a); Barucci et al. (2005); Birlan et al. (2006), spectral features were found which are similar to those of carbonaceous chondrites. This seems to hint at a more "primitive" surface composition, which is usually associated with a C-type classification and a geometric albedo below 0.1, incompatible with the IRAS value. Interestingly, Lupishko and Mohamed (1996) derived a geometric albedo of 0.100 from polarimetry. Also, Magri et al. (1999) found Lutetia's radar albedo to be the lowest measured for any M-type MBA—metallic objects are expected to display a high radar albedo. Furthermore, results of Rivkin et al. (2000) and Lazzarin et al. (2004a) indicate the presence of hydrated material on Lutetia's surface.

In short, the IRAS albedo seems incompatible with recent results. Barucci et al. (2005) thus called for a new determination of Lutetia's albedo.

We have observed Lutetia at visible and thermal-infrared wavelengths using the IRTF (see chapter 4). Data were analyzed using the NEATM (see sect. 2.5) and our TPM (see chapter 3).

Table 6.10: Observing geometry and modeling assumptions (H and G are from Tedesco, 1992).

Heliocentric distance r	2.065 AU
Geocentric distance Δ	2.199 AU
Solar phase angle α	27.4°
Absolute magnitude H	7.35
Slope parameter G	0.11
Thermal emissivity ϵ	0.9

Table 6.11: IRTF observations of 21 Lutetia. Times are those of mid exposure on June 24 2004 and are not light-time corrected. Filter "V" denotes an Apogee measurement; numbers denote the central wavelength (in µm) of the MIRSI filter used.

UT	Filter	Flux	σ_{Flux}
14:17	V	11.87 mag	0.01 mag
14:19	11.6	12.88 Jy	1.29 Jy
14:26	8.7	5.81 Jy	0.58 Jy
14:34	18.4	17.1 Jy	4.1 Jy
14:37	V	11.81 mag	0.01 mag

6.6.2 Observations

The observations were performed on June 24 2004, between roughly 14:15 and 15:00 UT, at the IRTF on Mauna Kea using the mid-infrared spectrometer and imager MIRSI (Deutsch et al., 2003, see also sect. 4.1.1) in imaging mode and the optical CCD Apogee (see sect. 4.1.2). Observing conditions were good with low humidity and no discernible clouds. See table 6.10 for the observing geometry.

We used three of MIRSI's narrow-bandwidth filters centered at 8.7, 11.6, and 18.4 µm (see also table 4.1 on p. 87). The photometry was calibrated against subsequent observations of the standard stars γ Aql and β Peg, for which absolutely calibrated spectra have been published by Cohen et al. (1996, 1999). We also obtained absolutely calibrated V-magnitudes of Lutetia just before and just after the MIRSI observations, using Apogee. These were calibrated against the Landolt (1973) standard star 93-101.

We used our IRTF data reduction techniques as described in sect. 4.4. See table 6.11 for a list of the optical and thermal-IR fluxes. For MIRSI N-band data (8.7 and 11.6 µm), the errors are dominated by the calibration uncertainty including possible atmospheric variability between observations; this uncertainty was estimated to be 10 %. For the Q-band filter centered at 18.4 µm, uncertainties
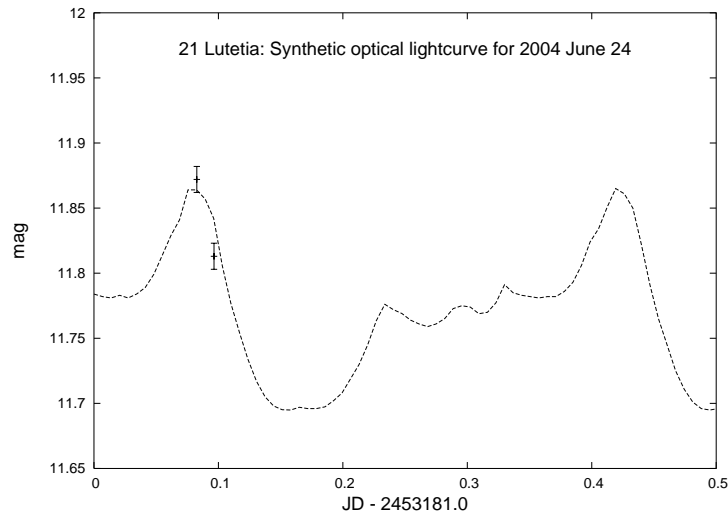
Figure 6.20: Measured V-band data (see table 6.11) and synthetic optical lightcurve generated using the shape model by Torppa et al. (2003). The rotational period is 8.165455 h, so some 1.5 cycles are displayed.

caused by the airmass correction and the statistical scatter resulting from the synthetic aperture procedure contributed an additional 14 % to the error budget.

6.6.3 Data analysis

6.6.3.a Observing geometry and rotational phase

From the inversion of multi-epoch optical lightcurves observed from 1962 through 1998, Torppa et al. (2003) derived a physical model of Lutetia's shape and spin state. Two pole directions are given, one of which seems to be superior to the other one (M. Kaasalainen, private communication, 2005). The J2000 ecliptic latitude of both solutions is $+3°$, the longitude is $39°$ for the preferred first solution and $220°$ for the secondary. This implies that during our observations, on 2004 June 24, the sub-Earth and subsolar latitudes were $-75°$ and $-48°$, respectively. Using the second pole orientation results in the same sub-Earth and subsolar latitudes, but with their signs changed.

The shape model of Torppa et al. (2003) was used to generate a synthetic optical lightcurve. In Fig. 6.20 the resulting lightcurve is plotted, together with our measured V-band data. Judging from Fig. 6.20 our observations took place near lightcurve minimum; the lightcurve amplitude is roughly 0.17 magnitudes from minimum to maximum.

Table 6.12: NEATM fits to the available thermal-infrared data: The MIRSI data as given in table 6.11, and the five IRAS sightings (Tedesco, 1992). No attempt at lightcurve correction was made.

	η	p_{V}	D (km)
MIRSI	0.93	0.188	103.8
IRAS 1	0.93	0.178	106.6
IRAS 2	0.94	0.226	94.7
IRAS 3	1.06	0.161	112.2
IRAS 4	0.96	0.191	103.0
IRAS 5	0.82	0.231	93.6

Table 6.13: NEATM diameters and albedos of Lutetia for the two data sets

	D (km)	p_{V}
MIRSI	104 ± 16	0.188 ± 0.057
IRAS (mean of five)	102 ± 16	0.197 ± 0.059

Between 1983 Apr 25 and May 4, Lutetia was sighted five times by IRAS (Tedesco, 1992); the observing geometry was practically constant, with a sub-Earth latitude of about 18° and a subsolar latitude of about -2°. Again, choosing the second pole solution changes the signs.

6.6.3.b NEATM

The NEATM (see sect. 2.5) was used to fit the MIRSI data (see table 6.11 on p. 184) and the IRAS flux values published by Tedesco (1992). IRAS was equipped with four broad-band filters centered at 12, 25, 60, and 100 µm. The filter breadth requires color corrections of the fluxes (Beichman et al., 1988);[12] we assumed a black-body temperature of 230 K. We considered only the 12, 25, and 60 µm filters since there are significant uncertainties concerning both the calibration of the 100 µm data and the applicability of the model at these wavelengths. All five IRAS sightings of Lutetia were used.

Throughout our data analysis we assumed Lutetia's thermal emissivity to be 0.9, and its absolute (optical) magnitude in the HG-system (Bowell et al., 1989) to be $H = 7.35$ with $G = 0.11$ (Tedesco, 1992).

See table 6.12 for an overview of the NEATM results. The mean results from the IRAS data are $p_{\mathrm{V}} = 0.197 \pm 0.027$, $D = 102.0 \pm 7.1$ km, and $\eta = 0.94 \pm 0.08$

---

[12] See also `http://irsa.ipac.caltech.edu/IRASdocs/exp.sup/ch6/tabsupC6.html`.
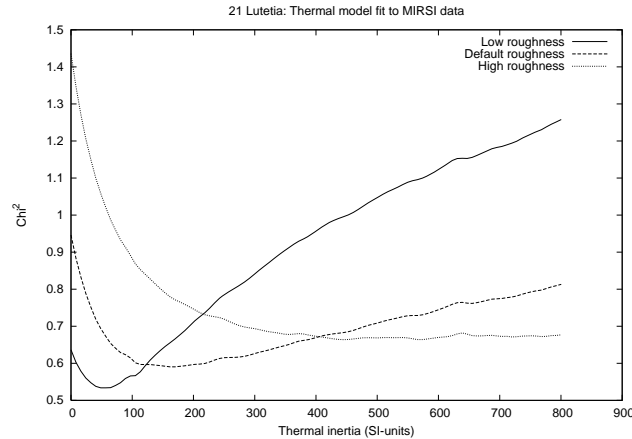
Figure 6.21: Goodness of fit χ^2 vs. thermal inertia for the MIRSI data. For each value of thermal inertia, the best-fitting diameter is found. The SI-unit of thermal inertia is $J\,s^{-1/2}K^{-1}m^{-2}$.

(errors are from the internal scatter only), in excellent agreement with our MIRSI results. We estimate that NEATM diameters and albedos are generally accurate to within 15 % and 30 %, respectively (see sect. 2.5.3). Our final results with conservative uncertainties are given in table 6.13.

We did not attempt to correct our data to the flux level of the lightcurve average; if the shape model by Torppa et al. (2003) adequately describes the epoch of our observations (see sect. 6.6.3.a), this should lead to a slight underestimation of the diameter of up to a few percent, well inside the range of uncertainty quoted.

Walker (2003) calculated a mean value for η of 1.067 ± 0.087 from IRAS observations of 694 asteroids. Our result for Lutetia, $\eta = 0.94 \pm 0.08$, is comparable to that of Walker, which indicates that Lutetia has thermal properties rather typical for a large MBA, i.e. low thermal inertia and some surface roughness.

6.6.3.c Thermophysical model (TPM)

We have analyzed our data using the detailed TPM (see chapter 3). We use the shape model by Torppa et al. (2003) discussed in sect. 6.6.3.a, which consists of a convex mesh of 2040 triangular facets.

It may not be appropriate to fit the MIRSI data with the TPM since its usage generally requires more than just three data points. As can be seen in Fig. 6.21, the best fit suggests low roughness and low thermal inertia of about 50 $J\,s^{-1/2}K^{-1}m^{-2}$,
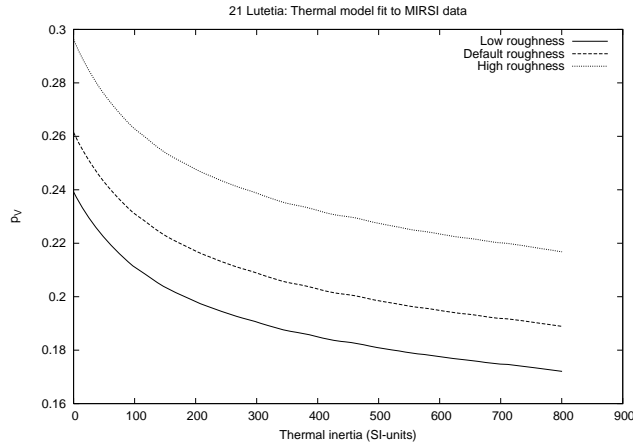
Figure 6.22: Best-fit geometric albedo p_V vs. thermal inertia for the MIRSI data; cf. Fig. 6.21.

about the thermal inertia of lunar soil. However, considerably higher thermal inertias can also be fitted by adding more surface roughness (note the scale on the χ^2-axis!). According to Müller and Lagerros (1998), typical MBA thermal inertias range between 5 and 25 J s$^{-1/2}$K^{-1}m^{-2}.

Nevertheless, as can be seen in Fig. 6.22, the best-fit geometric albedo p_V for the respective best-fit thermal inertia is largely independent of surface roughness: $p_V = 0.225 \pm 0.020$ and $D = 94.9 \pm 4.3$ km, in excellent agreement with our NEATM findings (sect. 6.6.3.b). The uncertainties quoted here reflect only the scatter of the fitting procedure; we estimate the systematic uncertainties inherent in the modeling and calibration to be significantly higher: 10 % for the diameter and 20 % for albedo. Our MIRSI data alone do not significantly constrain Lutetia's thermal inertia or surface roughness.

We have also used the TPM to fit the flux values measured by IRAS in 1983 (see sect. 6.6.3.b). As can be seen in Fig. 6.23, the IRAS data are also best fitted with a thermal inertia of about 50 J s$^{-1/2}$K^{-1}m^{-2}, however, this time the best fit is reached assuming high surface roughness rather than low surface roughness. The best-fit diameter and albedo are $p_V = 0.21 \pm 0.04$ and $D = 98.3 \pm 9.4$ km (statistical errors only, see above), in excellent agreement with our previous findings.

We have also attempted to simultaneously fit both data sets, MIRSI + IRAS. This leads to a best-fit thermal inertia of zero, whichever roughness is assumed. In particular, changing the roughness does not alter the goodness of the fit, so
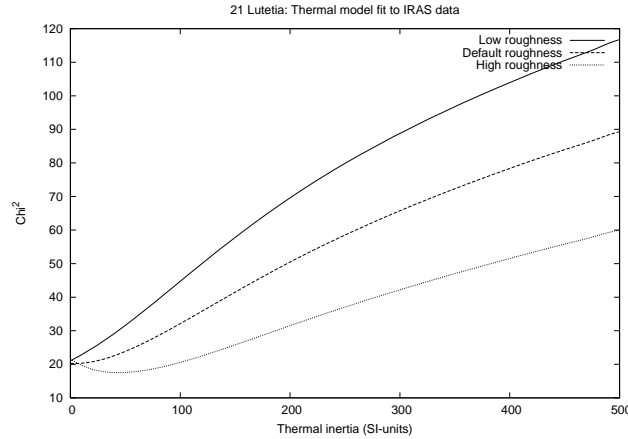
Figure 6.23: As Fig. 6.21, but for IRAS data.

roughness is not constrained at all. The corresponding diameter and albedo are $p_V = 0.235 \pm 0.027$ and $D = 92.9 \pm 5.4$ km (statistical errors only), in agreement with our previous findings.

While the TPM fits to the MIRSI, IRAS, and MIRSI + IRAS data sets give very similar values of D and p_V, results for thermal inertia and, in particular, surface roughness are not well constrained. However, our results strongly suggest that the thermal inertia does not greatly exceed 100 J s$^{-1/2}$K^{-1}m^{-2}.

Linking multi-epoch data taken some 20 years apart requires very accurate knowledge of the rotational period. The one used in this work (8.165455 h, Torppa et al., 2003) seems to be sufficiently accurate: it is based on a large temporal baseline of some 36 years (lightcurves from 1962–1998, including some from 1983), so it should safely bridge the six years 1998–2004. Judging from Fig. 6.20 on p. 185 this is indeed the case, although we caution that we have no more than two data points.

Another potential source of error is the sub-Earth latitude, which varies considerably between apparitions: in 1983, the sub-Earth latitude was +18°, as opposed to -75° in 2004 (see sect. 6.6.3.a). This could cause the shape model to be biased towards one hemisphere, although we note that lightcurves at various sub-Earth latitudes were used in the construction of the shape model (for example, the sub-Earth latitude in Oct. 1962 was -54°). Furthermore, the surface composition or roughness could vary across the surface; our model assumes it to be homogeneous.

Table 6.14: Summary of diameter and albedo determinations for Lutetia. Values in parentheses are calculated by us on the basis of eqn. 1.1 on p. 13 and $H = 7.35$. NEATM results are quoted with 15 and 30 % uncertainty in diameter and albedo, respectively; TPM results with 10 % uncertainty in diameter and 20 % uncertainty in albedo (see sect. 6.6.3.b and 6.6.3.c).

D (km)	p_V	Notes
95.8 ± 4.1	0.221 ± 0.020	Tedesco (1992, using the STM)
(142.4)	0.100	Lupishko and Mohamed (1996, from polarimetry)
116 ± 17	(0.151 ± 0.045)	Magri et al. (1999, from radar observations)
104 ± 16	0.188 ± 0.057	NEATM fit to MIRSI data
102 ± 16	0.197 ± 0.059	NEATM fit to IRAS data
94.9 ± 9.5	0.225 ± 0.045	TPM fit to MIRSI data
98.3 ± 9.9	0.210 ± 0.042	TPM fit to IRAS data
92.9 ± 9.3	0.235 ± 0.047	TPM fit to MIRSI+IRAS
98.3 ± 5.9	0.208 ± 0.025	Weighted average of rows 4–7

6.6.4 Discussion

6.6.4.a Diameter and albedo

We have determined the radiometric size and albedo of 21 Lutetia from two data sets (IRAS and new IRTF measurements) and two independent thermal models with different levels of sophistication, see sect. 6.6.3.b and 6.6.3.c. Given the progress since the IRAS results in both thermal modeling (Harris, 1998; Lagerros, 1998a) and mid-IR calibration (Cohen et al., 1996, 1999), our radiometric results should be more reliable than those of Tedesco (1992). Our results and those taken from the literature are summarized in table 6.14. Given the uncertainties, there is good mutual agreement among the radar results by Magri et al. (1999) and Tedesco's and our radiometric results, while the polarimetric albedo of Lupishko and Mohamed (1996) is inconsistent with all other albedo determinations. In particular, our results are incompatible with typical C-type albedos of ≤ 0.1, which may be indicated by recent spectroscopic findings (Birlan et al., 2004; Lazzarin et al., 2004a; Barucci et al., 2005).

6.6.4.b Thermal properties

From our data we have determined not only the radiometric diameter and albedo of Lutetia, but also the apparent color temperature, from which conclusions on the surface thermal properties, such as thermal inertia and roughness, can be drawn.

Using the NEATM, we found the fit parameter η, which describes the apparent color temperature, to be 0.93 / 0.94 for the MIRSI / IRAS-observations, respectively. This implies that Lutetia's thermal properties are rather typical for a MBA, i.e. low thermal inertia and some surface roughness.

Our results from the TPM confirm this picture in general: for both data sets, the best-fit thermal inertia is around 50 J s$^{-1/2}$K^{-1}m^{-2}, about the thermal inertia of lunar regolith and somewhat higher than the typical thermal inertia of large MBAs (Müller and Lagerros, 1998). Values in the range 0–100 J s$^{-1/2}$K^{-1}m^{-2} are consistent with our data. A larger data set would be required to conclusively determine Lutetia's thermal inertia.

6.6.5 Summary

From new thermal-infrared spectrophotometric measurements and detailed thermophysical modeling we infer that Lutetia has a diameter of 98.3 ± 5.9 km and a geometric albedo of 0.208 ± 0.025, in good agreement with the results from IRAS radiometry (Tedesco, 1992) and radar observations (Magri et al., 1999). We can rule out a low albedo typical of a C-type taxonomic classification as indicated by recent spectroscopic findings. Further spectroscopic observations should be made to check for variegation of spectral features with rotational phase and sub-Earth latitude.

Furthermore we confirm that Lutetia's surface must be covered with thermally insulating regolith. A lunar-like thermal inertia of 50 ± 50 J s$^{-1/2}$K^{-1}m^{-2} is compatible with both our MIRSI data and the IRAS flux values.

6.7 (10302) 1989 ML, potential Don-Quijote target [13]

The NEA (10302) 1989 ML is a nominal target of the planned ESA mission *Don Quijote*. To assist the target selection process, we were awarded Director's Discretionary Time with the Spitzer Space Telescope, which allowed us to determine the asteroid's size and albedo, critical parameters for mission planning. Combining our Spitzer results with optical and near-infrared data, we could furthermore classify 1989 ML as an E-type asteroid, thereby severely constraining its surface mineralogy.

---

[13] The content of this section was prepublished (Mueller et al., 2007). Only my contributions to that paper are presented herein.

6.7.1 Introduction

The most accessible asteroids for rendezvous missions are those with orbits similar to that of the Earth. Indeed, some NEAs are easier to reach than the Moon. The energy (Δv) and flight time required to reach the Amor-type NEA (10302) 1989 ML (period 1.44 yr, eccentricity 0.14, inclination 4.4°) are relatively small, comparable to those for the Hayabusa target (25143) Itokawa (Perozzi et al., 2001; Christou, 2003; Binzel et al., 2004), making it a very attractive spacecraft target for rendezvous missions. 1989 ML has been considered as a possible target for both the Japanese Hayabusa and the European Don Quijote missions (see Binzel et al., 2001; Harris et al., 2005b); at the time of writing further missions to NEAs are being planned in Japan, Europe, and the USA (see sect. 1.1), for which 1989 ML may be considered as a target. *However, a serious and urgent problem for mission planning is the lack of information on the physical properties of this asteroid.*

Preliminary optical lightcurve measurements by Weissman et al. (1999) and Abe et al. (2000) suggest the peak-to-peak amplitude is about 1 mag, corresponding to a very elongated shape. Weissman et al. report a rotation period near 19 h. However, according to Abe et al., ~ 32 h is also possible. This long-period high-amplitude lightcurve has limited the accuracy of determinations of the absolute optical magnitude, H: Abe et al. (2000) report $H = 19.7$ (assuming $G = 0.15$); NEODys (as of 18 April 2007) reports $H = 19.39$ ($G = 0.15$); Weissman et al. (1999) report an absolute magnitude in the R-band of $H_R = 19.14$, which implies $H = 19.47$ using $V - R = 0.37 \pm 0.03$ (Mueller et al., 2007). Since published H values for NEAs are notoriously unreliable, we adopt the average value of $H = 19.5$ with a conservative uncertainty of ± 0.3.

Binzel et al. (2001) report a neutral X_c-type spectrum at optical wavelengths, implying that 1989 ML belongs to one of the E, M, or P spectrally degenerate classes (see sect. 1.5.2). E-type asteroids have a high geometric albedo p_V ($0.3 < p_V < 0.6$) and may be related to enstatite achondrite meteorites; M-type asteroids have moderate albedos around 0.1–0.2 and some are probably related to metallic meteorites; P-type asteroids have very low albedos ($p_V \leq 0.1$) and appear to be organic-rich, similar to carbonaceous chondrites (see, e.g., Clark et al., 2004a,b). Determination of the albedo of an X-type asteroid is therefore very important for constraining its composition.

We observed 1989 ML in the thermal infrared using the Infrared Array Camera IRAC on board the Spitzer Space Telescope at a phase angle of 52.3°. We employed the NEATM (see sect. 2.5) to derive the effective diameter from the Spitzer data.

Table 6.15: Time-resolved flux densities of 1989 ML from IRAC channel 4 (7.872 µm) and observations 1–5. Flux values in parentheses are color corrected. Times refer to the beginning of the observation and are not light-time corrected.

JD - 2453889.0	Flux (µJy)	σ flux (µJy)
0.47827	126 (122)	19 (18)
0.60011	49 (47)	16 (15)
0.75043	115 (112)	23 (22)
0.86787	188 (182)	17 (16)
1.01833	91 (89)	21 (20)

6.7.2 Observations and data reduction

1989 ML was observed on 2006 June 2 and 3 with IRAC on board of Spitzer (see sect. 5.2). We were awarded a total of 1.2 h Director's Discretionary Time for this project.

The asteroid was observed six times, each observation providing nearly simultaneous photometry in all 4 IRAC channels with five dither positions, of 30 s integration time each, per field-of-view. The observation time in each case was about 12 minutes, including dead times for telescope slewing and settling, which is significantly shorter than the asteroid rotation period. In order to trace the rotational flux variability (about 1 mag at visible wavelengths) we requested time gaps (by imposing follow-on constraints on the individual observations) of ~ 3.2 h between consecutive observations, corresponding to $\sim 60°$ in rotational phase assuming the nominal rotation period of 19 h (Weissman et al., 1999). The observing geometry did not change significantly during our observations: the heliocentric distance was 1.270 AU, the distance to Spitzer was 0.891 AU, and the solar phase angle, α, was 52.3° (source: JPL Horizons System; all values are constant during our Spitzer observations to ± 2 in the last quoted digit or better).

We analyzed the obtained BCD images (see sect. 5.2.3) using the data reduction techniques presented in sect. 5.2.4. A discussion of the color corrections to the flux densities derived in this case is given in sect. 6.7.3.

The mosaics for observations 1–5 display clear asteroid signals at the predicted positions, but observation #6 failed, because the target asteroid was within $2''$ of a stellar background source of comparable brightness. Also data from observation #4 are compromised by the presence of a faint background source, which can be neglected for IRAC channels 3 and 4 but is comparable in flux to the asteroid at shorter wavelengths.

Table 6.16: Flux densities for all four IRAC channels derived from stacking observations 1–5. As in table 6.15, flux values in parentheses are color corrected.

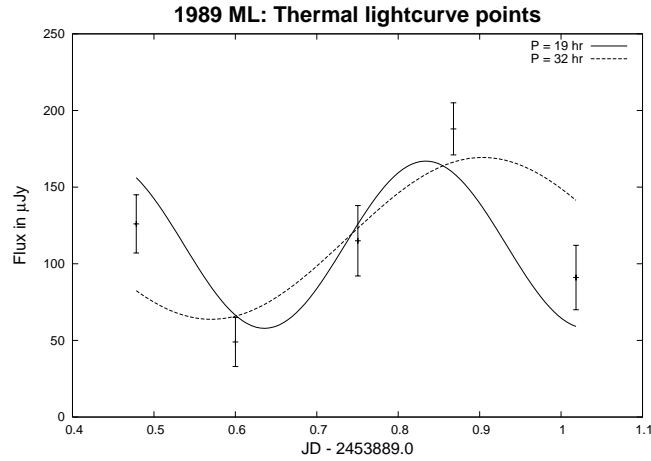| Central wavelength (µm)	Flux (µJy)	σ flux (µJy)
3.550	4.14 (4.14)	0.77 (0.77)
4.493	4.1 (3.8)	1.3 (1.2)
5.731	21.7 (20.3)	7.3 (6.8)
7.872	111.3 (108)	17.7 (18)

Figure 6.24: Time-resolved channel-4 data (not color corrected) as given in table 6.15 overlaid with two sinusoidal lightcurves corresponding to the rotation periods proposed in the literature. As is usual, the lightcurves are assumed to be double-peaked, i.e. the photometric periods equal half the rotation periods (9.5 and 16 h).

The highest signal-to-noise ratio is obtained in IRAC channel 4, from which photometry can be extracted for each observation yielding a coarse thermal lightcurve (see table 6.15). For all channels, we stacked images from observations 1–5 and derived an average flux value from the resulting mosaic images (see table 6.16).

6.7.3 Results

Our time-resolved channel-4 data given in table 6.15 (7.872 µm) are consistent with a high-amplitude long-period lightcurve as proposed in the literature. Sinusoidal double-peaked lightcurves corresponding to the two possible rotation periods of 19 and 32 h fit the data well, cf. Fig. 6.24. The average flux levels of the two
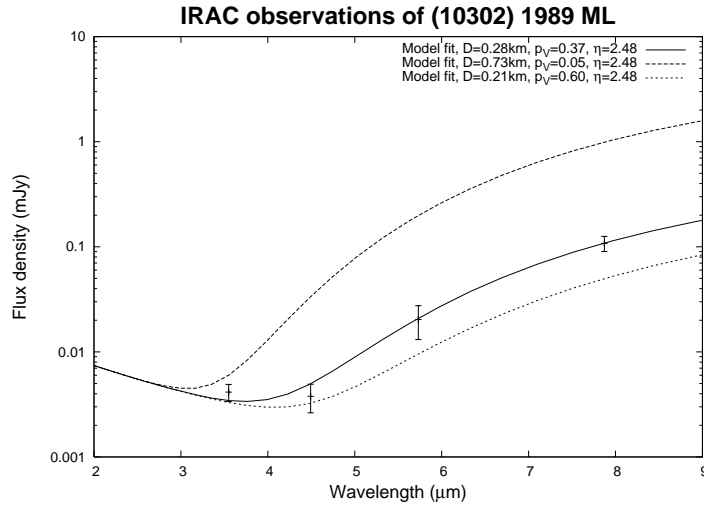
IRAC observations of (10302) 1989 ML

Figure 6.25: Model fits to the photometric data given in table 6.16. Both reflected sunlight and thermal emission are modeled (cf. text). The thermal contributions to channels 3 and 4 (wavelengths 5.7 and 7.9 µm) are fitted using the NEATM; the reflected sunlight is extrapolated from the predicted V magnitude assuming a relative reflectance of 1.2 (see text and Mueller et al., 2007, Fig. 2). An albedo of $p_V = 0.05$, which would be typical for P-type asteroids, is clearly incompatible with the data (dashed line).

fitted lightcurves are consistent with one another and with the flux value obtained from stacking images from observations 1–5 (table 6.16). Agreement is to within a few percent, a negligible difference compared to the statistical flux uncertainty. We cannot further constrain the rotation properties from our Spitzer data, but conclude that for all IRAC channels the flux values obtained from stacking observations 1–5 are good proxies to the lightcurve average flux level.

IRAC is a broad-band photometer, so the derived flux values must be color corrected (see sect. 5.2.4.g). Due to their different spectral shapes, different color corrections apply to the thermally emitted flux component and to reflected sunlight; color corrections to the latter are negligible. We estimated the amount of reflected sunlight in channels 1–4 assuming a solar black body temperature of 5800 K and a relative reflectance of ~ 1.2 between 3.6 µm and the V band (Mueller et al., 2007, Fig. 2). Reflected sunlight was found to contribute virtually all the measured flux in channel 1, only negligible amounts in channel 4, and ~ 1 µJy in channel 3 (~ 5 % of the measured flux). The relative contributions to the channel 2 flux cannot be easily determined.

We fitted the NEATM to the thermal flux values from channels 3 and 4 and calculated color-correction factors using the model parameters (diameter, p_V, and

η) derived. We repeated this procedure with color-corrected thermal fluxes, after which the procedure was seen to have converged; a second iteration brought about changes significantly below the 1 % level. The resulting model spectrum with the observational data overlaid is shown in Fig. 6.25.

The best-fit parameters are: Diameter $D = 0.276$ km, $p_V = 0.37$, and $\eta = 2.48$. Color-corrected fluxes were obtained by dividing the thermal flux contributions by 1.129 (channel 2), 1.070 (channel 4) and 1.034 (channel 4). Uncertainties in D, p_V, and η were estimated using a Monte-Carlo analysis. To this end, we generated a random set of synthetic thermal flux values at the channel-3 and channel-4 wavelengths, normally distributed around the measured values, and fitted them using the NEATM. We rejected unrealistic results with $\eta > 3$ or $p_V > 0.7$. The remaining sample of 15,000 results gave $D = 0.246 \pm 0.037$ km, $p_V = 0.46 \pm 0.13$, and $\eta = 2.23 \pm 0.44$ (1σ standard deviations—note, however, that the distribution of resulting model parameters is highly non-Gaussian). We adopt the fractional uncertainties from this simulation for our best-fit results stated above, yielding: $D = 0.276 \pm 0.041$ km, $p_V = 0.37 \pm 0.11$, and $\eta = 2.48 \pm 0.49$. The uncertainty in our adopted value for H (19.5 ± 0.3) contributes an additional 30 % to the albedo error (added in quadrature) so $p_V = 0.37 \pm 0.15$. This albedo is suggestive of an E classification. P types, for which p_V should not exceed 0.1, would appear to be ruled out (see also Fig. 6.25). We note that in addition to the statistical errors there is a systematic modeling uncertainty that increases with solar phase angle and thermal inertia (see Harris, 2006, and sect. 2.5.3), but in the sense of underestimating p_V. So the systematic uncertainty in the NEATM results in this case would tend to increase p_V above the value of 0.37 derived here.

Our albedo result is consistent with the available photometric and spectroscopic data in the optical and near-infrared wavelength ranges, which also favor an E-type classification (see Mueller et al., 2007, and references therein; that part of the paper is by co-author Prof. Fitzsimmons).

The derived η value of 2.5 ± 0.5 is rather high for a solar phase angle of $52°$ (Delbo' et al., 2003, see also Fig. 2.5 on p. 42) and is consistent with a high surface thermal inertia, corresponding to a lack of thermally insulating dust or regolith. Better spectral coverage and a thermophysical model would be required to derive conclusive statements about surface thermal properties.

6.7.4 Discussion

1989 ML is an attractive spacecraft target due to its low-Δv orbit. However, virtually no conclusive information on its physical properties has been available so far. Our determination of the object's size, albedo, and surface mineralogy is therefore helpful in the process of selecting suitable targets for NEA missions.

Knowledge on the target diameter is particularly mission relevant. Our result of $D = 0.276 \pm 0.041$ km is much lower than estimates based on the H value and common default values of p_V; e.g., assuming $p_V = 0.2$ results in a $\sim 35\%$ larger diameter, whereas the diameter of a P-type asteroid ($p_V \sim 0.05$) would be 2.7 times larger than our result. This corresponds to volume ratios of 2.5 or 20, respectively, and correspondingly large differences in mass. Constraints on the target mass are particularly important for the design of orbiting spacecraft.

For phase-A studies of the Don-Quijote mission, 1989 ML was chosen as one of two nominal targets (see, e.g., Harris et al., 2005b) assuming a diameter of 0.5 km, above our estimate by a factor of ~ 1.8 and corresponding to a ~ 6 times larger volume. Don Quijote consists of a kinetic impactor and an orbiter, its primary aim is to measure the impact-induced orbital change of the target NEA using the orbiter.

In the target definition process, it was found that a suitable target for Don Quijote should have a diameter up to 0.5 km in order to guarantee that the momentum transfer leads to an accurately observable change in orbit; we have found 1989 ML to clearly satisfy this constraint. On the other hand, too small asteroids do not allow stable spacecraft orbits around them and are harder to target with a kinetic impactor; note that a non-central impact would reduce the momentum transfered by ejecta. While no numerical value for a minimum diameter has been specified by Harris et al. (2005b), our results may imply that 1989 ML is too small to be considered a suitable target for Don Quijote.

Another target selection criterion for the Don Quijote mission is taxonomic type: Dark, C-type-like objects would be preferred (Harris et al., 2005b). With an albedo of $p_V = 0.37 \pm 0.15$, 1989 ML is clearly not a dark object.

6.7.5 Summary

On the basis of thermal-infrared photometric observations of the NEA (10302) 1989 ML using the IRAC camera on board the Spitzer Space Telescope we have determined its effective diameter to be 0.28 ± 0.05 km and its geometric albedo p_V

to be 0.37 ± 0.15. This high albedo is incompatible with a P-type classification, is only marginally consistent with an M-type classification, but is fully consistent with an E-type classification. The available optical and near-infrared data also favor E type. Taken together, we conclude that the available data suggest an E classification for (10302) 1989 ML—note that only 4 E-type NEAs were known beforehand (Clark et al., 2004a).

1989 ML is an attractive spacecraft target due to its Earth-like orbit. Virtually nothing was previously known about the physical properties of this easy-to-reach asteroid; our results will inform the target selection process of presently planned, and potentially of future NEA missions. In particular, we have found that the diameter of 1989 ML is much smaller than assumed in phase-A studies of the ESA mission Don Quijote. This, together with our result for its taxonomic type, most probably implies that 1989 ML is not a suitable target for Don Quijote.

6.8 Eclipses in the binary system (617) Patroclus

A particularly direct way of measuring thermal inertia is from time-resolved observations of the thermal response to eclipse events, effectively allowing one to see shadowed surface elements cool down and heat back up in real time. Recent progress in the orbital modeling of binary asteroid systems now allows the reliable prediction of eclipse events in such systems.

We here present the first thermal-infrared observations of an eclipsing binary asteroid system. Our target is the binary Trojan (617) Patroclus, which consists of two components of roughly equal size. The mutual orbit has been determined by Marchis et al. (2006), allowing them to determine the system's mass. Combining their result with a diameter estimate by Fernández et al. (2003), they determine the average mass density to be $0.8^{+0.2}_{-0.1}$ g cm^{-3}.

Using IRS on board the Spitzer Space Telescope, we have obtained a total of 18 thermal-infrared spectra ($\sim$ 8–33 µm) of the system, providing good temporal coverage of two mutual events in June 2006.

A preliminary analysis of the Spitzer data results in a thermal inertia of $\sim$ 90 J s$^{-1/2}$K^{-1}m^{-2}, slightly larger than that of Galilean satellites and significantly above published upper limits on the thermal inertia of two other Trojans. The latter are found to be methodologically unreliable. This is consistent with a relatively coarse regolith, coarser than on main-belt asteroids or our Moon.

The diameters of the two components are found to be 100 ± 10 and $108 \pm$

11 km, respectively, implying an average mass density of 1.15 ± 0.37 g cm^{-3}. This is consistent with the Marchis et al. estimate at the 1σ level but allows for a larger mass fraction consisting of rock and a lower porosity than estimated by Marchis et al. We wish to highlight the importance of accurate diameter estimation in the case of binary systems of known mass.

We caution that the results presented herein are based on a variant of the thermophysical model which is not yet fully tested. Furthermore, the Marchis et al. model of the mutual orbit is currently being refined on the basis of newly obtained observational data (Marchis, 2007, private communication); a final analysis of our data must await the availability of the latter.

6.8.1 Introduction

Thermal-infrared observations during eclipse events are a well-established technique to determine the thermal inertia of planetary satellites. E.g., Pettit and Nicholson (1930) determined the thermal inertia of our Moon from observations during a total lunar eclipse; Morrison and Cruikshank (1973) report observations of the Galilean satellites while the latter were eclipsed by Jupiter; Neugebauer et al. (2005) report observations of Iapetus during eclipses by Saturn's rings. Asteroids are not frequently shadowed by planets. Binary asteroid systems, however, are well known to undergo eclipses, when respectively one component shadows the other. Targeted observations of an eclipse event require the ability to predict its timing, which is reliably doable for only a handful of binary asteroid systems to date.

Our target, (617) Patroclus, is the only currently known binary system in the population of Trojans co-orbital with Jupiter (see sect. 1.2). Its two components have a diameter ratio around 1.1 and diameters around 100–120 km (see below). Trojan orbits are stable over most of the age of the Solar System (see Emery et al., 2006, and references therein). The origin of the Trojans is currently under debate, they may have originated at their present location or may have been captured during the epoch of the Late Heavy Bombardment (see sect. 1.2). Trojans have generally low albedos of $p_V \sim 0.04$ and virtually featureless, highly reddened reflection spectra in the visible and near-IR wavelength ranges; in both respects, they resemble cometary nuclei (e.g. Jewitt and Luu, 1990; Emery and Brown, 2003; Fornasier et al., 2004; Emery et al., 2006, and references therein). Trojans smaller than some 70 km in diameter appear to be collisional fragments, while larger bodies appear to be primordial "accretion survivors," i.e. bodies whose

current form and internal structure have remained unchanged since the time of their formation (Jewitt et al., 2000).

Patroclus was found to be binary by Merline et al. (2001). They determined the components' difference in near-IR brightness to be only 0.2 mag, implying a diameter ratio close to unity. The effective diameter of the (spatially not resolved) system was determined by Tedesco et al. (2002a) to be 140.9 ± 4.7 km (based on IRAS observations analyzed using the STM—see sect. 2.4.1), corresponding to a geometric albedo of $p_V = 0.047 \pm 0.003$ with an absolute optical magnitude of $H = 8.19$. Fernández et al. (2003) obtained new 12.5 µm observations of Patroclus at the Keck II telescope. Using the STM, they reproduced the IRAS result, but rejected it in favor of a diameter of 166.0 ± 4.8 km ($p_V = 0.036 \pm 0.004$) based effectively on the NEATM (see sect. 2.5) assuming $\eta = 0.94$, which they argue is more representative of Trojans than the STM value of $\eta = 0.756$. It is worth pointing out that the quoted uncertainties solely reflect the statistical uncertainty although there are considerable systematic uncertainties, due mostly to the uncertainty in η. This is acknowledged by Fernández et al. to limit the accuracy of their results, but no quantitative discussion of the systematic uncertainty is given. Note that the quoted diameters are area-equivalent diameters $D_\mathcal{A}$ of the system as a whole. $D_\mathcal{A}$ is related to the components' diameters, D_1 and D_2, through $D_\mathcal{A}{}^2 = D_1{}^2 + D_2{}^2$.

The system's mutual orbit was determined by Marchis et al. (2006) based on spatially resolved adaptive-optics observations. They report a purely Keplerian orbit (without precession) to fit their data well. The best-fit orbit is roughly circular (eccentricity 0.02 ± 0.02) with a center-to-center separation of the two components of 680 ± 20 km, corresponding to a maximum angular separation around $0.2''$. The J2000 ecliptic coordinates of the spin pole are $\lambda = 234 \pm 5°$, $\beta = -62 \pm 1°$, the orbital period equals 102.8 ± 0.1 h. Combining their result with the size estimate by Fernández et al., Marchis et al. infer a mass density of only $0.8^{+0.2}_{-0.1}$ g cm^{-3}, compatible with a composition dominated by water ice and moderate porosity. The size uncertainty accounts for most of the uncertainty in the mass density. The brightness ratio of the two components was found by Marchis et al. to be roughly identical for two different near-IR filters, indicative of an identical surface mineralogy. Assuming identical albedo, they infer a diameter ratio of 1.082 and, using the Fernández et al. size estimate, diameters of 112.6 and 121.8 km for the two components, respectively.

Optical lightcurve observations (Angeli et al., 1999, Mottola, unpublished work)

reveal a low amplitude indicative of roughly spherical components. The spin properties of the individual components are not well constrained, but there is no indication for multi-periodicity in the available lightcurve data which were taken at epochs when no mutual events occurred. This is consistent with a synchronization of the individual spin periods with the orbital period, possibly through tidal damping.

The orbit model by Marchis et al. (2006) allowed a series of mutual events in 2006 to be predicted. A large campaign has been launched for targeted observations of these events using optical telescopes. The orbit model is currently being refined on the basis of data obtained in the course of that campaign (Marchis, 2007, private communication).

We used the InfraRed Spectrograph (IRS; see sect. 5.3) on board the Spitzer Space Telescope to observe two eclipse-occultation events in June 2006, where one component obstructed the line of the sight from the other component towards the Sun and the observer, respectively. A total of 18 spectra ($\sim$ 8–33 µm) was obtained, nine per event, providing good temporal coverage.

Our thermophysical model (TPM) was generalized to allow for the effects of eclipses and occultations (see chapter A in the appendix). Applying the generalized TPM to our Spitzer data, we could determine the thermal inertia of the Patroclus system in a way which is nearly unaffected by systematic uncertainties due to thermal-infrared beaming (see sect. 3.2.3). This represents the first determination of an asteroid thermal inertia from eclipse observations and the first reliable determination of the thermal inertia of a Trojan. We furthermore determine the size and albedo of the object, allowing us to refine the mass-density estimate by Marchis et al. (2006).

We caution that the generalized TPM is not yet fully tested; moreover, the orbit model of the Patroclus system, on which our modeling is based, is currently being refined (see above). All results presented in this section are therefore preliminary.

6.8.2 Observations

Patroclus was observed using the InfraRed Spectrograph (IRS) on board the Spitzer Space Telescope. IRS was used in "low-resolution" spectroscopy mode (see sect. 5.3.3) using the modules SL1, LL1, and LL2 (see table 5.12 on p. 134) to obtain spectra in the nominal wavelength range 7.4–38 µm at a relative spectral resolution $\lambda/\Delta\lambda$ between 64 and 128. The observed flux is practically purely thermal. The angular separation of the two components of the Patroclus sys-

Table 6.17: (617) Patroclus: Times of our Spitzer observations. There were nine observations per event, referred to as 1.0–1.8 and 2.0–2.8, respectively. Times refer to the beginning of the observations measured at Spitzer. Each observation ended after about 6 min.

	Day (June 2006)	Time (UT)		Day (June 2006)	Time (UT)
1.0	24	18:40	2.0	26	10:42
1.1	24	21:54	2.1	26	23:22
1.2	24	22:47	2.2	27	00:24
1.3	24	23:54	2.3	27	01:31
1.4	25	00:41	2.4	27	02:19
1.5	25	01:47	2.5	27	03:29
1.6	25	02:49	2.6	27	04:24
1.7	25	04:12	2.7	27	05:55
1.8	25	05:24	2.8	27	06:52

tem is never larger than $0.2''$ (and minimized during occultations) while the IRS pixel scale is $1.8''$ or coarser (see table 5.12 on p. 134), hence the system was not spatially resolved.

Time-resolved observations were obtained during two consecutive mutual events in June 2006, referred to as events 1 and 2 in the following. In event 1, the larger component shadowed the smaller, and vice-versa in event 2. The diameter ratio is only ~ 1.1 and the mutual orbit is roughly circular, hence the two events produced very similar observable effects. Both events were combined eclipse-occultation events and lasted about 6.5 h; the predicted chronology of event 2 is:

June 26, 23:15 UT: Start of the eclipse

June 27, 02:45 UT: Start of the occultation (eclipse ongoing)

June 27, 05:45 UT: End of the event

The 1σ timing uncertainty is ~ 30 min, much more accurate predictions are expected from the refinement of the orbit model, which is currently under development.

A total of 18 thermal-infrared spectra of Patroclus has been obtained, nine per event, providing good temporal coverage of both events and their aftermath (see table 6.17 for the observation times and table 6.18 for the observing geometry). To enable comparison, two observations were performed before the predicted start of

Table 6.18: (617) Patroclus: Observing geometry at the epoch of our observations: heliocentric distance r, Spitzer-centric distance Δ, solar phase angle α, and J2000 ecliptic coordinates (longitude and latitude) in a heliocentric and Spitzer-centric frame, respectively. All values are constant during our observations to ± 1 in the last quoted digit or better. The absolute optical magnitude equals $H = 8.19$ (quoted after Tedesco et al., 2002a), the slope parameter $G = 0.15$.

Event:	1	2
r	5.947 AU	5.947 AU
Δ	5.95 AU	5.98 AU
α	9.80°	9.77°
Heliocentric	170.8°, +18.03°	170.9°, +18.00°
Spitzer-centric	160.5°, +18.2°	160.7°, +18.1°

the events (observations 1.0 and 2.0), while the purpose of the observations after the end of the events (1.7–1.8, 2.7–2.8) was to observe the heating up of the system.

To prevent wavelength-dependent spill-over losses, IRS spectroscopy targets must be accurately centered into the slit. The projected width of the LL slits is above $10''$, while that of the SL1 slit is $3.7''$ (see table 5.12 on p. 134), comparable to the width of the point-spread function (PSF) in the respective wavelength range. "Blind" telescope pointings have a 1σ-accuracy of $0.5''$ and are therefore adequate to center sources of well known position (such as Patroclus) in the wide LL slits but risk placing large portions of the PSF outside the SL1 slit. IRS has an automated peak-up mechanism (see sect. 5.3.1) to refine the pointing based on imaging with dedicated peak-up detectors. This mechanism could not be used for our observations, however, because Patroclus would have saturated the peak-up detectors. Instead, small spectral maps were created for the SL1 observations, with three small steps perpendicular to the slit, each offset by $2''$ (roughly half the slit width). This enables one to estimate the target offset from the slit center and to correct for the effects thereof in the data analysis (this strategy was developed and previously used by our colleague J. Emery, see Emery et al., 2006).

The apertures of the used IRS modules have a projected length of $57''$ or more, hence one-dimensional spatial information can be obtained in addition to the spectral dimension. The usual "nod" strategy was used, i.e. the target was placed at about 33 and 66 % of the slit length in each module in order to enable subtractive correction for diffuse background emission ("sky background"). The spectral maps for the LL observations consist of two pointings for the two nod positions, that for the SL1 observations consists of a total of 6 positions (two nod positions
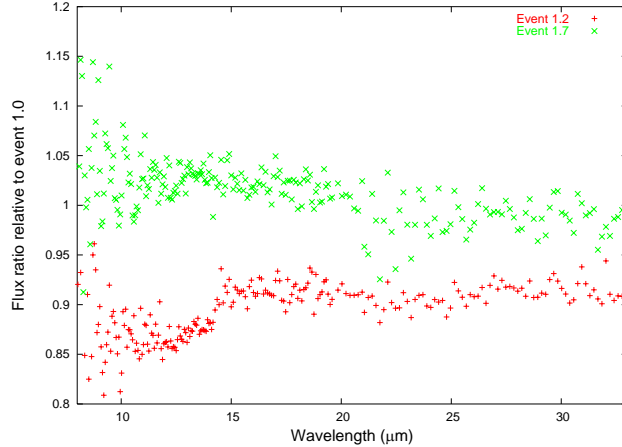
Figure 6.26: (617) Patroclus: Ratio of two measured thermal spectra relative to pre-event measurement 1.0. Observation 1.2 was taken during the eclipse, observation 1.7 in the aftermath. Note the difference in flux level and spectral slope, which is consistent with the eclipse-induced temperature drop!

times three pointings perpendicular to the slit).

The obtained data have been reduced by Emery using the methods described in Emery et al. (2006, sect. 3). The detectors contain permanently and temporarily damaged pixels, which required measurements for some wavelengths to be excluded from further consideration, e.g. all wavelengths above 33 µm. For each data point, the statistical flux uncertainty is estimated based on photon count statistics and the observed difference between the two nod positions. Data from the different IRS submodules (which have some spectral overlap) were multiplicatively matched to one another. Systematic flux uncertainties due to, e.g., the residual effect of source mis-centering or uncertainties in the absolute flux calibration are estimated to be 3 % (see, e.g., table 5.13 on p. 135) and added in quadrature. The total flux uncertainty is dominated by the systematic uncertainty except for the Wien slope at the shortest wavelengths.

See Fig. 6.26 for a representative plot of flux ratios during event 1.

The observed spectra contain slight spectral features due to silicates within the wavelength ranges 10–12 µm and 18–22 µm (Emery, 2006, private communication). In order to avoid biases, those wavelengths were disregarded in the following, leaving 179 data points per observation.

6.8.3 NEATM analysis

As a first step, the obtained spectra were analyzed using the NEATM (see sect. 2.5); see Fig. 6.27 for results from the nine observations of event 1, results for event 2 are qualitatively identical. Observations 1.7 and 1.8, which were obtained after the end of the event, imply an effective diameter around 147 km and $\eta \sim 0.88$, intermediate between previous estimates by Tedesco et al. (2002a) and Fernández et al. (2003). During the events, there is a clearly recognizable dip in best-fit diameter which reflects the event-induced flux drop. Simultaneously, the best-fit η rises (with the exception of observation 1.1), corresponding to a lower apparent color temperature due to the eclipse-induced cooling of the shadowed parts.

While the NEATM takes no direct account of shadowing or occultation, the NEATM results clearly indicate that we have indeed observed the thermal response to mutual events.

6.8.4 Thermophysical modeling

In order to obtain a reliable estimate of the thermal inertia and diameter, the data were analyzed using a generalized thermophysical model (TPM) (see chapter A in the appendix). In the modeling of shadowing effects and thermal inertia, the spin axis position (Marchis et al., 2006) and the observing geometry (see table 6.18 on p. 203) are explicitly taken into account. Thermal-infrared beaming is modeled in terms of a "beaming factor" η (see sect. A.1.5) which is not to be confused with the NEATM η (the latter accounts for the *combined* effect of thermal inertia and beaming, rather than for beaming alone). The Patroclus system is assumed to be tidally locked and on a circular mutual orbit, such that the system is at rest in a co-rotating frame (see sect. A.1.2); this is consistent with all available data (see sect. 6.8.1—the orbital eccentricity of 0.02 ± 0.02 is negligible). Both components are assumed to be spherical and homogeneous in terms of mass density, albedo, roughness, and thermal inertia.

The timing uncertainty, which was estimated to be ± 30 min before the Spitzer observations, is non-negligible compared to the event duration of ~ 6.5 h, requiring a non-standard fit technique to be used: Variable model parameters are the time offset Δt, thermal inertia Γ, beaming parameter η, and area-equivalent diameter $D_{\mathcal{A}}$ (see sect. 2.2.1 for a definition and eqn. A.2 on p. 249). Patroclus' albedo is very low, $p_V \sim 0.04$, so its absorptivity (on which temperatures depend) is close to unity. Consequently, temperatures are virtually independent of the precise
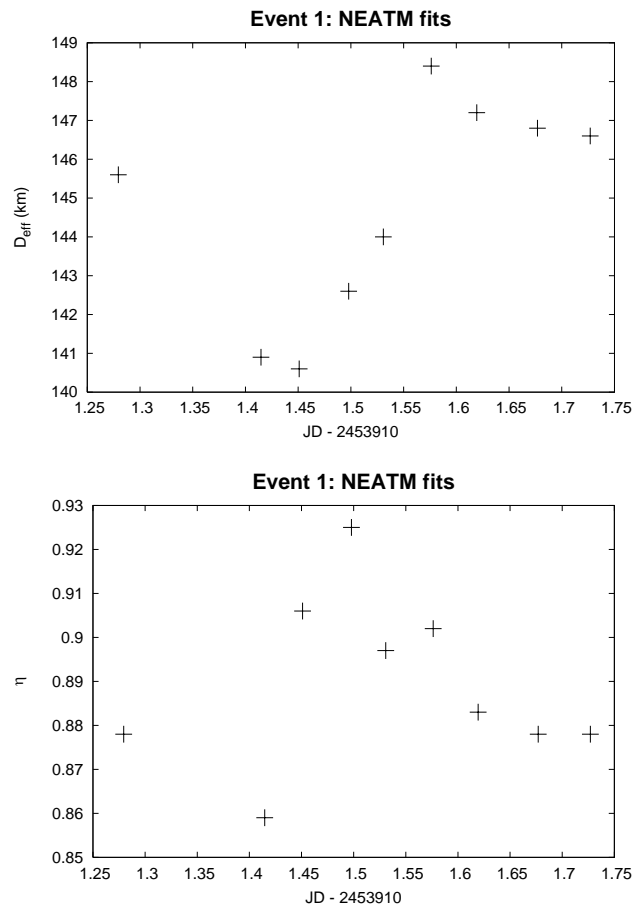
Figure 6.27: (617) Patroclus: NEATM fits to spectra for event 1. Above: Best-fit effective diameter against observing time. Below: Best-fit η against observing time.

Table 6.19: (617) Patroclus: Best-fit TPM parameters for events 1 and 2 (average and standard deviation of 5000 Monte-Carlo runs; see text). Δt is given in units of h, thermal inertia in units of J s$^{-1/2}$K^{-1}m^{-2}, $D_{\mathcal{A}}$ in km. The total number of data points per event is $9 \times 179 = 1611$, hence the reduced χ^2 equals $\chi^2/1607$ (there are four fit parameters).

	Reduced χ^2	Δt	Γ	η	$D_{\mathcal{A}}$
Event 1	14.2 ± 0.2	-0.47 ± 0.02	89 ± 3	0.62 ± 0.00	149.5 ± 0.4
Event 2	5.6 ± 0.2	-1.02 ± 0.02	90 ± 4	0.62 ± 0.01	144.6 ± 0.4

value of p_V (see Fig. 3.2 on p. 67). Model fluxes were calculated for $p_V = 0.041$ (corresponding to $D_{\mathcal{A}} = 151.054$ km assuming $H = 8.19$) and later rescaled with a spectrally constant factor κ (see below) to vary the diameter.

Synthetic lightcurves were generated for the wavelengths at which data had been obtained (disregarding the position of spectral features; see above) and for different values of thermal inertia and η. Fluxes were calculated for 1000 time points per revolution, corresponding to a time resolution of ~ 6 min or roughly the length of one Spitzer observation. After initial runs over wider and coarser grids of Γ and η values, an equidistant grid was considered with Γ varying between 14 and 110 J s$^{-1/2}$K^{-1}m^{-2} (step width 3 J s$^{-1/2}$K^{-1}m^{-2}) and η between 0.56 and 0.95 (step width 0.03), totaling to 462 Γ–η combinations.

Data were analyzed separately for each event. To this end, model fluxes were interpolated for the times of the respectively nine observations plus a variable time offset Δt. Initial runs showed the required range in Δt to be -1.5—0 h (i.e. events occured somewhat earlier than predicted), the resolution of the Δt grid was 2 min. For each combination of Γ, η, and Δt, a flux-scale-factor κ was found which minimizes χ^2 (see eqn. 2.17 on p. 45); κ and the corresponding χ^2 were stored. After searching the grid, that combination of Γ, η, and Δt was determined which lead to the global minimum in χ^2. The corresponding best-fit diameter equals 151.054 km $\times \sqrt{\kappa}$ (fluxes are proportional to D^2).

In order to study the accuracy of the results, a Monte-Carlo technique was employed: For each event, 9×5000 random spectra were generated, normally distributed around the measured data. Best-fit parameters were determined for each set of nine random spectra; see table 6.19 for their mean values and standard deviations.

We note that the standard deviations of the best-fit values are much lower than realistic expectations on the accuracy of our results, particularly so for η. This may indicate an underestimation of the flux uncertainty, which would also be

consistent with the fact that our values for the reduced χ^2 significantly exceed unity. Alternatively, we may be unable to resolve the true uncertainties if they are comparable to the resolution of the search grid used by us. A detailed analysis of the uncertainties is deferred to a later stage, when the improved orbit model will be available. Keeping this in mind, we conclude that the best-fit Γ, η, and $D_{\mathcal{A}}$ for the two events are in excellent agreement with one another. The two values for the best-fit diameter average to 147 km, in excellent agreement with the NEATM analysis (see sect. 6.8.3). The best-fit thermal inertia is 90 ± 4 J s$^{-1/2}$K^{-1}m^{-2}, where the uncertainty is likely to be underestimated. The best-fit TPM η is 0.62, significantly below the best-fit NEATM η. This is consistent, given the fact that the TPM η only reflects the effect of beaming, rather than the combined effect of thermal inertia and beaming as its NEATM counterpart. The found η value suggests a very rough surface, probably even rougher than the lunar surface (for which $\eta \sim 0.72$; Spencer et al., 1989).

Results for the best-fit time offset Δt for the two events differ at a statistically significant level: Apparently, both events took place earlier than predicted, by ~ 0.5 h in the case of event 1, ~ 1.0 h in the case of event 2. The discrepancy of 0.5 h corresponds to a rotational phase $< 2°$. We note that the orbit model by Marchis et al. (2006) has a slight eccentricity of 0.02±0.02 which is neglected in our thermophysical modeling. We speculate that this caused the slight discrepancy in timing offsets.

Additional simulation runs were performed in which the components were assumed to be biaxial ellipsoids rather than spheres. Their longest axes were assumed to be aligned with one another and with the line connecting the two components; this is the stable attractor state of such a system. Axis ratios (identical for the two components) of 1.03, 1.06, and 1.09 were tried, leading to very similar results compared to the spherical case. Larger axis ratios would appear to be inconsistent with the observed low lightcurve amplitude.

6.8.5 Discussion

Diameter and mass density   Two independent analyses of the data (using the NEATM and the TPM) resulted in a best-fit diameter of $D_{\mathcal{A}} \sim 147$ km; the corresponding albedo is $p_{\mathrm{V}} = 0.0433$. This is intermediate between previous estimates by Tedesco et al. (2002a) and Fernández et al. (2003). Note that in the derivation of both, the apparent color temperature (effectively: η) was not derived but rather assumed. Our result, on the other hand, is based on data with broad wavelength

coverage, allowing us to determine the color temperature reliably. Consequently, our results would be expected to be more reliable.

The systematic diameter uncertainty inherent in the TPM is hard to estimate in a quantitative way. In the case of near-Earth asteroids, it was found not to exceed 10 % (see sect. 7.2). Thermophysical modeling of Patroclus, with roughly spherical components and observed at low phase angles $< 10°$, would appear to be much less challenging (apart from the effect of mutual events) and potentially more accurate. We conclude that 10 % is a conservative upper limit on the diameter uncertainty.

The diameters of the components are 100±10 and 108±11 km, respectively. This corresponds to a total volume of $(1.18\pm0.36)\times10^6$ km^3, implying an average mass density of 1.15 ± 0.37 g cm^{-3}. This is consistent at the 1σ level with the previous estimate by Marchis et al. (2006). In particular, it seems that the accuracy of the Fernández et al. (2003) diameter estimate was overestimated.

We wish to stress the importance of accurate diameter measurements of binaries: Since the mass density is linear in mass but inversely cubic in diameter, mass densities are particularly susceptible to diameter uncertainties; e.g., a diameter uncertainty of 15 % translates into a mass-density uncertainty around 45 %. For this reason, the uncertainty in mass density is typically limited by diameter inaccuracies (see Merline et al., 2002; Richardson and Walsh, 2006).

Thermal inertia   We derive a thermal inertia of ~ 90 J s$^{-1/2}$K^{-1}m^{-2} for the Patroclus system. The uncertainty is hard to estimate in a quantitative way, but the good mutual agreement between results for the two events and the very low scatter found in a Monte-Carlo analysis (see table 6.19) are reassuring.

As expected, the measured thermal inertia is much below that of bare rock (2500 J s$^{-1/2}$K^{-1}m^{-2}) implying the existence of a thermally insulating layer of regolith. However, our result is significantly larger than the value for lunar regolith (50 J s$^{-1/2}$K^{-1}m^{-2}; see, e.g., table 3.1 on p. 58) or for large main-belt asteroids, which average around 15 J s$^{-1/2}$K^{-1}m^{-2} Müller and Lagerros (1998). This suggests a relatively coarse regolith.

It must be taken into account that the heliocentric distance of Patroclus is $r \sim 6$ AU, hence its surface is much colder than, e.g., that of the Moon. In general, thermal inertia is temperature dependent; for purely radiative heat conduction (as expected for fine regolith) thermal inertia would be expected to scale with $r^{-3/4}$ (see sect. 7.3.2). Under this assumption, the thermal inertia of Patroclus at a

Table 6.20: Small Solar-System bodies beyond the asteroid main belt: Overview of previously published estimates of thermal inertia. KBO is for Kuiper belt object.

	Thermal inertia $(\mathrm{J\ s^{-1/2}K^{-1}m^{-2}})$	Reference
(617) Patroclus (Trojan)	~ 90	This work
(2363) Cebriones (Trojan)	< 14	Fernández et al. (2003)
(3063) Makhaon (Trojan)	< 30	Fernández et al. (2003)
Ganymede (Jovian satellite)	~ 70	Spencer (1987)
Callisto (Jovian satellite)	~ 50	Spencer (1987)
Europa (Jovian satellite)	45–70	Spencer et al. (1999)
(8405) Asbolus (Centaur)	< 11	Fernández et al. (2002)
(2060) Chiron (Centaur)	3^{+5}_{-3}	Groussin et al. (2004)
(10119) Chariklo (Centaur)	0^{+2}_{-0}	Groussin et al. (2004)
(55565) 2002 AW197 (KBO)	< 20	Cruikshank et al. (2005)
(134340) Pluto (KBO)	30–50	Lellouch et al. (2006)

heliocentric distance of 1 AU would be around 350 $\mathrm{J\ s^{-1/2}K^{-1}m^{-2}}$, comparable to our findings for the typical thermal inertia of near-Earth asteroids (see sect. 7.3.1). While this appears to be somewhat surprising, an analysis of spectral features found in our data also indicates the presence of a coarse regolith (Emery, 2007, private communication).

Our thermal-inertia result is significantly above published upper limits on the thermal inertia of two other Trojans (Fernández et al., 2003, see also table 6.20). We note that the latter are based on a significantly less extensive database and were obtained using an indirect method: Fernández et al. found their data to be more consistent with the STM than with the FRM (see sect. 2.4). From this they conclude that the thermal parameter (see eqn. 3.10c on p. 55) should be ≤ 1 (no quantitative discussion is given) which they transform into an upper limit on thermal inertia. In their analysis, the effect of thermal-infrared beaming is neglected; at the small phase angles at which Trojans are observed, beaming increases the apparent color temperature while thermal inertia lowers it. Moreover, the spin axis orientation of their targets is unknown, they appear to assume equatorial aspect. Both beaming and non-equatorial aspect reduce the observable effect of thermal inertia, and would therefore increase thermal-inertia estimates derived from any given data set. The upper limit published by Fernández et al. (2003) is therefore methodologically unreliable. While it remains unclear how representative Patroclus is of the Trojan population as a whole, we conclude that the typical thermal

inertia of Trojans appears to be much larger than previously thought.

It is instructive to compare our result to thermal-inertia estimates for other atmosphereless bodies in the outer Solar System, although we caution that their surface composition may be very different from that of Trojans.

Since thermal parameters are temperature dependent (see above), the probably best analogues are the satellites of Jupiter, with which the Trojans are co-orbital. Using close-up spacecraft observations in the thermal infrared, Spencer (1987, using Voyager data) and Spencer et al. (1999, using Galileo data) determined the thermal inertia of three Galilean satellites, superseding previous estimates by Morrison and Cruikshank (1973). Their results (see table 6.20) are only slightly lower than our result, hence the surface of Patroclus may be expected to resemble those of Galilean satellites. We caution that the dynamics of ejecta, which are likely to be crucial for the formation of regolith, are very different on planetary satellites compared to asteroids (see also sect. 7.3.3.d). Furthermore, Jovian satellites as opposed to Trojans are significantly influenced by absorption of Jovian emission.

There are published estimates of the thermal inertia of three Centaurs (see table 6.20). Centaurs are icy planetoids which orbit the Sun between the orbits of Jupiter and Neptune, at typical heliocentric distances between 5 and 30 AU. Some Centaurs display cometary activity near perihelion (e.g. Tholen et al., 1988). The upper limit on the thermal inertia of Asbolus reported by Fernández et al. (2002) is based on an analysis analogous to that by Fernández et al. (2003) (see above) and would therefore seem equally unreliable. Assuming a spin axis perpendicular to the respective orbital plane, Groussin et al. (2004) estimate the thermal inertia of the nuclei of the active Centaurs (2060) Chiron and (10119) Chariklo. Some observational evidence is provided for the assumed equatorial aspect in the case of Chiron, but not for Chariklo. We conclude that Groussin et al.'s thermal-inertia estimate for Chiron appears to be reliable while that for Chariklo seems unreliable. It is intriguing that the thermal inertia of a Centaur should be so much lower than Patroclus'.

Cruikshank et al. (2005) report Spitzer observations of the Kuiper belt object (55565) 2002 AW197 at a heliocentric distance of 47.15 AU. They used the Spencer (1990) TPM to derive an upper limit of 8.7 J s$^{-1/2}$K^{-1}m^{-2} on this object's thermal inertia assuming equatorial aspect and an upper limit on the rotation period of 154 h. Unfortunately, nothing is known about the pole orientation of this object, not even its rotation period is known. Nevertheless, Cruikshank et al. conclude that the thermal inertia of 2002 AW197 is likely to be "well below

20" J s$^{-1/2}$K^{-1}m^{-2}. Assuming thermal conduction to be dominated by radiative heat transfer, the corresponding thermal inertia at a heliocentric distance of 1 AU would be $<$ 360 J s$^{-1/2}$K^{-1}m^{-2}, again comparable to our results for near-Earth asteroid and Patroclus.

The thermal inertia of Pluto has been measured by Lellouch et al. (2006) based on extensive Spitzer observations (refining a previous estimate by Lellouch et al., 2000, which was based on ISO observations). Pluto's spin state and shape are well known, hence we would consider the results of Lellouch et al. reliable. Note, however, that the thermal conduction on Pluto would be expected to be enhanced by its thin atmosphere, hence its thermal inertia cannot be readily compared to that of atmosphereless bodies.

Model assumptions   The thermophysical modeling is based on the orbit model by Marchis et al. (2006) which is currently being refined (see sect. 6.8.1). The slight orbital eccentricity of 0.02 ± 0.02 is neglected, i.e. the mutual orbit is assumed to be circular. Furthermore, the system is assumed to be tidally locked, which is consistent with all observational data known to us.

We caution that the spin states of the components are presently not well constrained. Furthermore, our results indicate that the orbital eccentricity has an influence on the event timing and may have an influence on the event geometry (although results from the mutually independent analyses of the two events are in otherwise excellent agreement). Orbital eccentricity induces a slight time variability in the orbital distance of the two components. An improved modeling approach, in which orbital eccentricity would be included to first order, would be to use two different models of the systems for the two events: In each, the mutual orbit would remain circular (as required by our current TPM, see sect. A.1.2) but the orbital distance would be different for the two events; those distances would need to be determined from the future refined orbit model.

Both components are assumed to have a spherical shape. This is expected to be a fair approximation given the reportedly low lightcurve amplitude at epochs when no mutual events occur. The TPM allows for ellipsoidal shapes, first model simulations with different axis ratios were seen to result in virtually identical results.

Mass density, albedo, surface roughness, and thermal inertia are assumed to be homogeneous over the Patroclus system. While this is a nontrivial assumption, spatially resolved observations of the two components through different filters re-

veal a roughly constant brightness ratio (Merline et al., 2001; Marchis et al., 2006), consistent with our assumption. It is also supported by the good mutual agreement of the independent analyses of the two observed events: Although the system was not spatially resolved, the observed eclipse-induced system would be expected to depend primarily on the eclipsed component. Vast component-to-component differences in physical properties would be expected to lead to inconsistencies which were not observed.

The approximate modeling of thermal-infrared beaming is expected to be uncritical, given the small phase angle ($< 10°$) at which our observations took place.

6.8.6 Summary

We report the first thermal-infrared observations of an eclipsing binary asteroid system, the Trojan (617) Patroclus. A total of 18 thermal spectra ($\sim$ 8–33 µm) were obtained using the IRS on board the Spitzer Space Telescope, providing good temporal coverage of two mutual events but no spatial resolution. The data were analyzed using a thermophysical model in which the effects of the eclipse-occultation geometry, thermal conduction, and thermal-infrared beaming are taken into account.

We derive the first reliable estimate of the thermal inertia of a Trojan, $\Gamma \sim$ 90 J $s^{-1/2}K^{-1}m^{-2}$. This is comparable to the thermal inertia of Galilean satellites and indicative of a relatively coarse regolith. However, our result is much larger than previous estimates of the thermal inertia of two Trojans which we found to be methodologically unreliable.

The diameters of the two components have been determined to be 100 ± 10 and 108 ± 11 km, respectively; the accuracy of previously available estimates was overestimated. Our result implies an average mass density of 1.15 ± 0.37 g cm^{-3} (using the mass estimate by Marchis et al., 2006); the quoted uncertainty is conservative.

6 Results

214